

Key Engineering Materials

Volume - 12

Issue No. 1

January - April 2024



ENRICHED PUBLICATIONS PVT.LTD

**JE - 18,Gupta Colony, Khirki Extn,
Malviya Nagar, New Delhi - 110017.**

E- Mail: info@enrichedpublication.com

Phone :- +91-8877340707

Key Engineering Materials
Managing Director
Amit Prasad

Key Engineering Materials

(Volume - 12, Issue No. 1, January - April 2024)

Contents

Sr. No.	Articles / Authors Name	Pg. No.
1	Friction: From Leonardo Da Vinci to Modern Nanotechnologies <i>- A V Makarov</i>	1 - 6
2	Structural and Micromechanical Properties of 316L stainless Steel Produced by Selective Laser Melting <i>- A V Makarov, V P Kuznetsov, V A Sirosh, E G Volkova, P A Skorynina and A G Merkushev</i>	7 - 12
3	Ultrasonic Welding of Metals: Instruments, Process Parameters, and Prospects of Welding of Ultrafine Grained Materials <i>- A A Mukhametgalina, M A Murzinova, A A Nazarov, N Yu Parkhimovich, A A Samigullina, E R Shayakhmetova and A P Zhilyaev</i>	13 - 20
4	Nano-Mechanical Testing of Al-Nb Metal Matrix Composites Consolidated by High Pressure Torsion after Annealing <i>- R R Mulyukov, K S Nazarov, R U Shayakhmetov, G F Korznikova, E A Korznikova</i>	21 - 26
5	Size-Dependent Phase Stability of Silver Nanoparticles <i>- A M Murzakaev</i>	27 - 31

Friction: From Leonardo da Vinci to Modern Nanotechnologies

A V Makarov

M.N. Miheev Institute of Metal Physics, Ural Branch of the Russian Academy of Sciences, 18 S. Kovalevskoy St., Ekaterinburg, 620108, Russia E-mail: avm@imp.uran.ru

ABSTRACT

The review paper presents an outstanding contribution of Leonardo da Vinci to the science of friction, which is the heart of modern nanotechnologies. It demonstrates a significant role of nanocrystalline friction structures (NCFS) in the formation of the tribological properties of metal alloys and in the implementation of deformation-induced nanostructuring techniques for metal alloy surface processing. Inherent in the very nature of friction, the ability to obtain an NCFS can be effectively used for targeted nanostructuring of product surface layers in order to increase their resistance to wear, corrosion, mechanical loads, and high temperatures. This can be achieved by using simple frictional and ultrasonic impact-frictional surface treatments, as well as combined methods based on the chemical modification of the formed NCFS. It is proposed to use nanostructuring frictional pretreatment and the industrial technology of nanostructuring burnishing in combined methods for surface preparation of structural stainless steels, including those produced by additive laser technology, for applying high-strength nanocomposite thin-film coatings.

1. INTRODUCTION

Along with gravitation, friction is the most important process largely determining life on the Earth. A fundamental contribution to the understanding and application of the phenomenon of friction was made by Leonardo da Vinci (1452–1519), a great thinker, scientist, and artist. This became especially evident in 1960s, after two of his unpublished manuscripts, known as the Madrid Codices, had been sensationally found in the Madrid National Library. The great Leonardo “pronounced a sentence” to the perpetual motion machine – many years before the official refusal of the French Academy of Sciences to accept for consideration perpetuum mobile projects as unscientific since frictional losses are inevitable. 200 years before Amonton’s experiments and almost three centuries before the publication of Coulomb’s studies, Leonardo da Vinci, basing himself on experiments, discovered the basic laws (aspects) of friction, introduced the notion of the friction coefficient into engineering practice, proposed antifriction bronze – the copper and tin alloy similar to the low-melting-point bearing alloy patented by Babbitt in 1839, invented a very complicated globoid gear, discovered anew only two and a half centuries later [1].

In fact, it is friction that underlies effective methods for surface nanostructuring of metals and alloys. Inherent in the very nature of friction is such important condition for deformation-induced nanostructuring as the formation of the stress state implemented during shearing under high pressure.

And what about Beilby layers appearing during metal polishing, having high hardness, chemical stability, and adsorptivity? These layers (and G. T. Beilby discovered them as early as in 1921) had for a long time been classed as amorphous materials, and it was not before the development of transmission electron microscopy that researchers managed to reveal superfine (nanocrystalline) structure of the Beilby layers. It may have been these manifestations of the frictional effect (friction) that ushered in the era of nanotechnologies.

This review paper, based on studies by the author and his associates, briefly analyzes one of the acute and practically important problems of physical metallurgy, namely studying and using nanocrystalline friction structures (NCFS).

2. FEATURES OF NCFS FORMATION IN METALS AND ALLOYS

Nanocrystalline friction structures form naturally in thin surface layers of metals and alloys. They result from a specificity of the stress arising in the friction contact zone. Microvolumes of the metal in the surface layers of the rubbing bodies are affected by external contact shear and compressive stresses. This creates conditions for extremely large values of plastic strain to occur in a 1–10 μm thick layer, which are reachable only under conditions of rotational plasticity, which causes the NCFS formation [2, 3]. NCFSs appear both under sliding friction and under abrasive action in the process of coarse-crystalline (figure 1 a) structure evolution during the sequential implementation of the sliding and twinning mechanisms, the formation of banded (figure 1 b) and cellular (figure 1 c) substructures, ultrafine textured (figure 1 d) and, at the final stage, nanocrystalline (figure 1 e, f) structures with large-angle misorientations of crystallites sized up to 100 nm [4–6]. Effective metal nanostructuring is promoted by a high friction coefficient (to enhance shear strain) and a noncorrosive environment in the friction contact zone (to prevent oxygen-induced embrittlement of the diffusively active nanostructured layer) [3, 5–7].

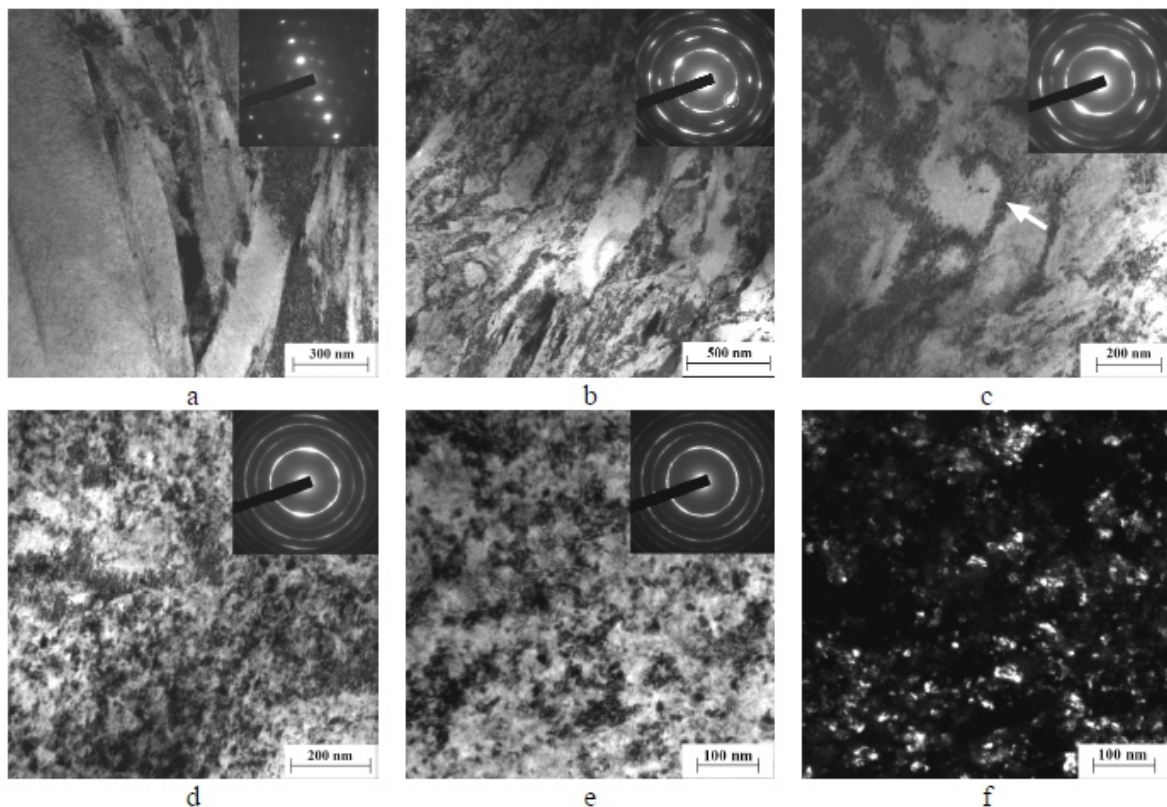


Figure 1. The structure of the 80S4 steel (0.85% C; 4.20% Si) (a) after water quenching from 870°C and cold treatment at –196°C and (b–f) subsequent frictional treatment: (a–e) bright-field images and microdiffractions; (f) dark-field image taken in the (110) α reflection.

3. NCFS CONTRIBUTION TO THE FORMATION OF THE TRIBOLOGICAL PROPERTIES OF METAL ALLOYS

The strength characteristics (microhardness, shear strength) and tribological (Latin tribos – friction) properties (friction coefficient and wear rate) of NCFS are largely governed by the level of their dispersion, the conditions of dislocation displacement through the bulk of the nanograins, the resistance

of NCFS fragments to rotations, the presence of interstitial elements (carbon, nitrogen), the degree of alloying with substitutional elements, the type of the crystal lattice, the presence of dispersed strengthening phases (carbides, nitrides, intermetallics), the magnetic state of austenite, and the effect of the air environment causing NCFS fracture due to oxygen-induced embrittlement [2, 3, 5].

Thus, in low-alloy (<0.1% C) iron alloys, the NCFSs of γ (FCC) austenite and ϵ (HCP) martensite demonstrate a much higher resistance to adhesive wear than the NCFS of α (BCC) martensite, whose wear resistance increases sharply during alloying with substitutional elements (Si, Ti) enhancing the solid-solution strengthening of martensite. The factors decreasing NCFS viscosity, such as the presence of relatively brittle intermetallic (Ni₃Ti, Ni₃Al) and ϵ -carbide particles and oxygen saturation of the active surface layer, negatively affect the resistance of steels and alloys to wear. In alloys with a high (~0.8%) carbon or nitrogen content, the maximum strength and resistance to adhesive wear are characteristic of the NCFS of high-carbon α -martensite since the impurity mechanism of dislocation pinning by carbon atoms in the NCFS of α -martensite is more effective than in the NCFS of austenite.

Low values of the friction coefficients ($f = 0.25\text{--}0.28$) and high resistance to adhesive wear are characteristic of the NCFS of the ϵ (HCP) phase of high-manganese iron alloys, including steels, and the NCFS of the γ (FCC) phase of nitrogen-containing austenitic steels. This is due to the effect of slight basal slip in the crystals (fragments) of the NCFS ϵ -phase, isomorphous to α -cobalt, as well as to the degeneration of multiple slip and the intensification of planar slip in NCFS fragments of nitrogen austenitic steels.

4. USING NCFSS IN MODERN DEFORMATION NANOTECHNOLOGIES

The indisputable scientific and practical significance of studying NCFSs stems not only from their important contribution to the formation of the tribological properties steels and alloys. The next logical step was intentional formation of a stable nanostructured layer with improved characteristics of wear resistance, heat resistance, corrosion resistance, and mechanical strength on the surfaces of metal products. This is achieved by the application of fairly easy-to-implement frictional treatments (figure 2), enabling even the surfaces of difficult-to-deform steels (laser-quenched, cemented, high-speed) to be nanostructured [5, 6, 8, 9]. For effective implementation of this method of nanostructuring and strengthening, it is necessary to provide strain accumulation in a thicker surface layer without its accelerated destruction (wear) during frictional treatment proper and to decrease the hazard of premature brittle failure of “over-work-hardened” nanostructured layer as early as in the initial operation period.

It is important to note the high potential of practical application of frictional treatments as finishing nanostructuring techniques for producing surfaces with low roughness [10–14]. The metal-physical foundations of frictional treatment find application in the manufacturing technology of nanostructuring burnishing, which is successfully implemented in multifunction turn-milling centers [10, 11]. The proposed ultrasonic impact-frictional treatment (UIFT) is an effective development of ultrasonic treatments [15–19]; as distinct from the standard ultrasonic impact treatment (UIT), it is performed by the method of oblique impact of a pulsing indenter and without using a lubricant (figure 3). This treatment makes it possible to increase the shear component of plastic strain owing to the enhanced friction effect on the metal. This facilitates strain accumulation within a layer and, correspondingly, more effective dispersion of the structure (up to the nanoscale) and steel surface layer strengthening.

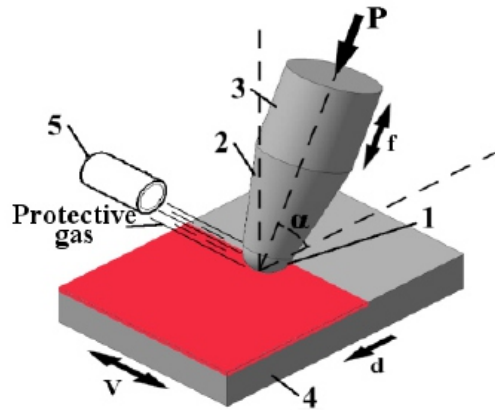
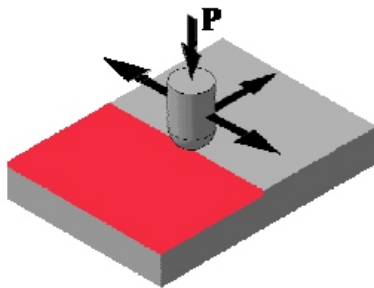


Figure 2. Scheme of frictional treatment. Figure 3. Scheme of UIFT: 1 – tool (indenter); 2 – wave guide; 3 – magnetostrictive or piezoelectric transducer; 4 – specimen; 5 – tube for protective gas feeding.

5. FRICTION NANOSTRUCTURING USED IN COMBINED TECHNOLOGIES OF MODIFYING METAL ALLOY SURFACES

NCFs formed by frictional treatment are effective in combined deformation-thermal treatments of martensitic [20–22] and austenitic [18, 23] steels, laser-clad Cr-Ni coatings [24], as well as in deformation-thermochemical treatments, particularly, in the intensification of the processes of low-temperature plasma nitriding [25–28]. The accelerated diffusion of elements over the crystal defects NCFs is provided by their high imperfection, namely long grain and subgrain boundaries, extreme density of dislocations, disclinations, and pin-hole defects.

The application of frictional treatment [6, 18] and the manufacturing technology of nanostructuring burnishing [10, 11] with sliding indenters for the formation of nanocomposite superhard and heat-resistant zirconium-carbonitride- and chromium-aluminum-based coatings on the surface of austenitic metastable [13] and deformation-resistant [29] steels seems to be promising. It is expedient to use nanostructuring burnishing in combinations with plasma nitriding as the postprocessing of stainless steels, produced by the additive laser technology, for subsequent application of nanocomposite thin-film multilayer coatings based on amorphous superhard diamond-like carbon and titanium carbides.

The essence of the proposed new approaches lies in overcoming the basic disadvantage of dead-hard and superhard thin-film coatings consisting in their low toughness and high brittleness. This manifests itself in coating cracking and the loss of adhesion to the base when coatings are applied onto products with rather low hardness. Therefore, it is proposed to apply coatings onto a surface pre-strengthened by friction. Such a combination of methods will allow us to obtain a synergic effect by summing and enhancing the advantages of separate methods, namely high surface hardness and a gradient transition from the surface to the base. The significance and relevance of the proposed line of research result from a matchless opportunity to expand the area of application for state-of-the-art nanocomposite coatings on relatively soft structural steels, including those synthesized by the additive technology of selective laser melting (SLM).

6. CONCLUSION AND PROSPECTS

Leonardo da Vinci made a fundamental contribution to the understanding and application of the phenomenon of friction. An important manifestation of friction in metal alloys is the formation of nanocrystalline friction structures (NCFs) in their surface layer, which result from the development of rotational plasticity.

The presented analysis of NCFs, based on publications by the author and his associates, not only promotes the state-of-the-art development of the metal-physical foundations of the friction and wear of metal alloys, but also creates prerequisites for the improvement of already known methods of strain hardening and combined strengthening of metal surfaces with elements of friction-induced nanocrystallization, as well as for the appearance of new ones. The paper notes the high effectiveness of frictional treatment, the proposed ultrasonic impact-frictional treatment, and combined deformation thermal (thermochemical) treatments aimed at the nanostructuring of steels and alloys and for the improvement of their operationally important properties.

Of particular scientific and practical interest are the prospects of using NCFs in new combined technologies for the formation of nanocomposite thin-film coatings with improved operational properties on austenitic stainless steel surfaces, as well as in combined post-treatments of maraging and austenitic steel products made by additive laser techniques. The stated problem can be solved by combined treatments including frictional deformation (frictional treatment and nanostructuring burnishing), possible additional plasma nitriding followed by the deposition of nanocomposite superhard, dead-hard, and heat-resistant coatings.

Acknowledgments

The research was carried out within the state assignment of Ministry of Science and Higher Education of the Russian Federation (theme "Structure" No. AAAA-A18-118020190116-6), supported in part by RFBR and Sverdlovsk Oblast (project No. 20-48-660065) and by RFBR and BRFR (project No. 20-58-00057). The studies were performed at the collaborative access center "Testing center of nanotechnology and advanced materials" of the M.N. Mikheev Institute of Metal Physics of the Ural Branch of the Russian Academy of Sciences (IMPUB RAS).

REFERENCES

- [1] Silin A A, ed. 1983 *Trenie i Ego Rol` v Razvitiu Tekhniki (Moscow: Nauka Publ.)* p 176 [in Russian]
- [2] Korshunov L G, Makarov A V and Chernenko N L 1994 *Fizika Metallov i Metallovedenie* 78 128 [in Russian]
- [3] Korshunov L G, Makarov A V and Chernenko N L 2000 *Phys. Met. Metallogr.* 90 S48
- [4] Makarov A V, Korshunov L G, Schastlivtsev V M, Solodova I L and Yakovleva I L 2004 *Phys. Met. Metallogr.* 98 428
- [5] Makarov A V and Korshunov L G 2004 *Russ. Phys. J.* 47 857
- [6] Makarov A V and Korshunov L G 2019 *Phys. Met. Metallogr.* 120 303
- [7] Makarov A V, Savrai R A, Pozdejeva N A, Smirnov S V, Vichuzhanin D I, Korshunov L G and Malygina I Yu 2010 *Surf. Coat. Technol.* 205 841
- [8] Makarov A V and Korshunov L G 2003 *Trenie i Iznos (Friction and Wear)* 24 301
- [9] Makarov A V, Korshunov L G, Vykhodets V B, Kurennykh T E and Savrai R A 2010 *Phys. Met. Metallogr.* 110 507
- [10] Kuznetsov V P, Makarov A V, Kiryakov A E, Savrai R A and Anikeev A V 2012 Patent RF 2458777
- [11] Kuznetsov V P, Makarov A V, Psakhie S G, Savrai R A, Malygina I Yu and Davydova N A 2014 *Phys. Mesomechanics* 17 250
- [12] Makarov A V, Skorynina P A, Osintseva A L, Yurovskikh A S and Savrai R A 2015 *Obrabotka Metallov (Tekhnologia, Oborudovaine, Instrumenty)* 4(69) 80 [In Russian]
- [13] Makarov A V, Skorynina P A, Yurovskikh A S and Osintseva A L 2017 *Phys. Met. Metallogr.* 118 1225

-
-
- [14] Savrai R A, Makarov A V, Malygina I Y and Volkova E G 2018 *Mater. Sci. Eng. A* 734 506
- [15] Makarov A V, Malygina I Yu, Burov S V and Savrai R A 2018 Patent RF 2643289
- [16] Makarov A V, Savrai R A, Malygina I Yu, Volkova E G and Burov S V 2018 *AIP Conf. Proc.* 2053 020006 5 p
- [17] Lezhnin N V, Makarov A V and Luchko S N 2019 *Letters on Materials* 9 310
- [18] Makarov A V, Savrai R A, Skorynina P A and Volkova E G 2020 *Met. Sci. Heat Treat.* 62 61
- [19] Lezhnin N V, Makarov A V, Luchko S N, Loginov B A and Loginov A B 2020 *Obrabotka Metallov (Tekhnologia, Oborudovaine, Instrumenty)* 22(2) 16
- [20] Makarov A V, Korshunov L G, Malygina I Yu and Solodova I L 2007 *Metal Sci. Heat Treat.* 49 150
- [21] Makarov A V, Savrai R A, Gorkunov E S, Yurovskikh A S, Malygina I Yu and Davydova N A *Phys. Mesomechanics* 2015 18 43
- [22] Makarov A V, Korshunov L G, Savrai R A, Davydova N A, Malygina I Yu and Chernenko N L 2014 *Phys. Met. Metallogr.* 115 303
- [23] Makarov A V, Skorynina P A, Volkova E G and Osintseva A L 2018 *Phys. Met. Metallogr.* 119 1196
- [24] Makarov A V, Soboleva N N and Malygina I Yu 2017 *AIP Conf. Proc.* 1915 030012 5 p
- [25] Makarov A V, Gavrilov N V, Samoylova G V, Mamaev A S, Osintseva A L and Savrai R A 2017 *Obrabotka Metallov (Tekhnologia, Oborudovaine, Instrumenty)* 75 55
- [26] Makarov A V, Samoiloa G V, Gavrilov N V, Mamayev A S, Osintseva A L, Kurennykh T E and Savrai R A 2017 *AIP Conf. Proc.* 1915 030011 5 p
- [27] Lezhnin N V, Makarov A V, Gavrilov N V, Osintseva A L and Savrai R A 2018 *AIP Conf. Proc.* 2053 040050 5 p
- [28] Zhidkov I S, Kukhareno A I, Makarov A V, Savrai R A, Gavrilov N V, Cholakh S O, Kurmaev E Z 2020 *Surf. Coat. Technol.* 386 125492
- [29] Makarov A V, Skorynina P A, Volkova E G and Osintseva A L 2020 *Met. Sci. Heat Treat.* 61 764

Structural and Micromechanical Properties of 316L Stainless Steel Produced by Selective Laser Melting

A V Makarov¹, V P Kuznetsov^{1,2}, V A Sirosh¹, E G Volkova¹, P A Skorynina³ and A G Merkushev²

¹M .N. Miheev Institute of Metal Physics, Ural Branch of the Russian Academy of Sciences, 18 S. Kovalevskoy St., Ekaterinburg, 620108, Russia

²Ural Federal University, 19 Mira St., Ekaterinburg, 620002 Russia

³Institute of Engineering Science, Ural Branch of the Russian Academy of Sciences, 34 Komsomolskaya St., Ekaterinburg, 620049, Russia

E-mail: sirosh@imp.uran.ru

ABSTRACT

The structure and micromechanical properties of a 316L stainless steel produced by the selective laser melting (SLM) technique have been studied in its initial state and the following heat treatment: quenching from 1050 °C and 4-hour annealing at 480 °C. The heat treatment does not result in changing the steel phase composition, however, it reduces the microhardness by 5%, HM hardness (Martens hardness) by 12% and indentation hardness by 16% at HIT maximum load. The heat treatment also increases the E* contact elasticity modulus by 14% due to the lower porosity of the material. As soon as heat treatment provides no strengthening of the steel synthesized by SLM, deformation processing, chemicothermal treatment and application of thin coatings may become quite promising strengthening methods.

1. INTRODUCTION

Additive manufacturing has been gaining a solid ground in modern engineering. This rapidly progressing technology proves to be the most promising for the fabrication of complex parts in the aeronautic, automotive, medical industries, etc. Selective laser melting is one of its applications, which is the layer-after-layer formation of a piece by laser beam scanning of powder layers laid on a substrate. As layers are added, different parts of the piece are subjected to various thermal effects. This leads to residual stresses caused by temperature gradients between the layers. This effect is likely to initiate cracking and delamination of the material [1]. The combination of incomplete fusion [2] and residual stresses brings about high porosity inside the part. Hence, the application of post-processing (deformation processing, heat and chemicothermal treatments, deposition of coating) designed to improve the quality of the material is topical for parts synthesized by the SLM technique.

The purpose of the study was looking into the structural phase states and micromechanical characteristics of stainless chrome-nickel steel samples produced by SLM, including those that were subjected to post-heat treatment.

2. MATERIALS AND METHODS

Stainless austenitic steel samples produced by SLM were studied, their chemical composition being (mass) Cr 15.93%; Ni 10.00%; Mo 2.20%; Mn 1.27%; Si 0.55%; C 0.03%; S 0.02%; P 0.08%, Fe – the rest. An EOS M 280 unit was used to build the samples in gaseous nitrogen employing a 400W laser; the diameter of the laser spot on the surface was 50µm, the thickness of the applied powder layer - 20µm, the rate of the laser beam movement on the powder surface reaching 1000 mm/sec. The structure and micromechanical properties of the steel were investigated in its initial state after forming the samples by the SLM technique and subsequent heat treatment. The aim of heat treatment (HT) was to degass and reduce the amount of vacancies, and to relax residual stresses in the synthesized sample.

It was heat treated at 1050 °C for 30 minutes, followed by oil quenching with subsequent 4-hrs ageing at 480 °C and air cooling.

A JEOL JEM-200CX transmission electron microscope was used to study the steel structure. To determine the microhardness, a Shumadzu HMV-G21DT device as well as the residual imprint method were utilized with a load on the Vickers indenter of 0.245 N. An ISO 14577 Fischerscope Hm2000 XYm measurement system was applied to determine the microindentation characteristics. The maximum microindentation load on the Vickers indenter was 0.245 N. The micromechanics of the coatings were found with the help of loading and unloading curves gained by the Oliver-Pharr method [3].

3. EXPERIMENTAL RESULTS AND DISCUSSION

The transmission electron microscope survey showed that the initial structure of the 316L steel samples in the planes cut parallel (∥) and perpendicular (⊥) to the Z axis (figure 1), i.e. parallel and perpendicular to the sample building direction during the SLM process, prior to the heat treatment was identical. The structure consists of elongated subgrains with separate dislocations or dislocation cells inside them (figure 2). All the grains were γ -Fe (austenite).

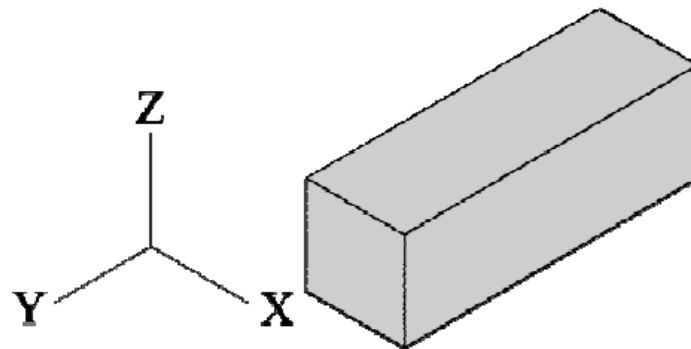


Figure 1. Schematic illustration of the sample synthetization: X,Y - scanning direction, Z - building direction.

The structure of the heat-treated steel in the vertical plane parallel to the Z axis, i.e. in the direction of the sample building (∥), comprises elongated austenitic subgrains with prolonged, straight, bandshaped boundaries (figure 3). The density of dislocations inside the grains is low.

The results of the structural survey fully agree with the published data on the cellular structure in 316L stainless steel formed by SLM [4-6]. The 30 minutes annealing at 1050 °C prior to quenching is expected to make gaseous impurities, which are likely to have evolved during the SLM process, to emit from the γ -solid solution [6]. Uneven distribution of powder in SLM could have led to the formation of the ferrite phase [7], but no α -phase was detected.

The microhardness tests applying the recovered indentation technique revealed that heat treatment results in a slight softening of the steel; the microhardness decreased by 5% from 252. \pm 7 HV 0.025 to 240. \pm 5 HV 0.025.

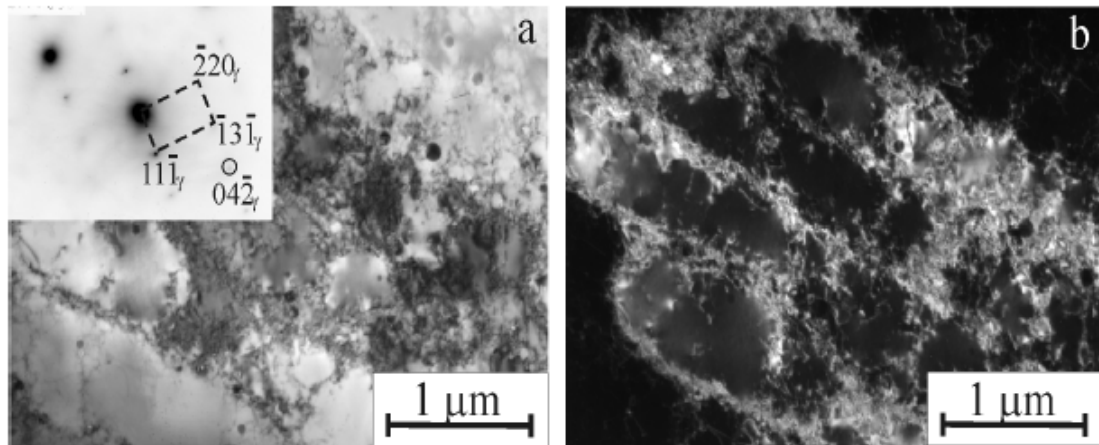


Figure 2. TEM images of the initial 316L (II) SLM samples structure: bright field and electronic diffraction patterns (a), dark field (b).

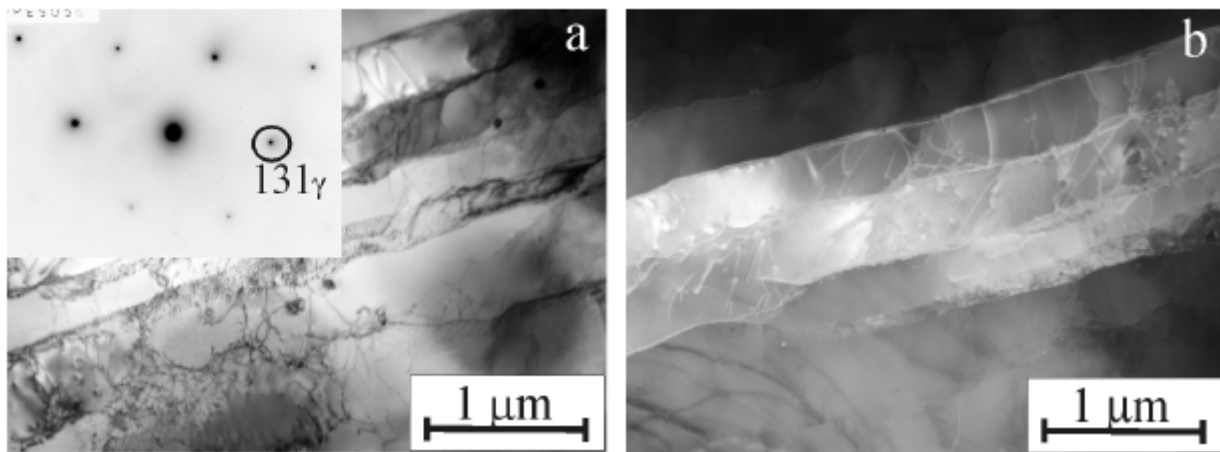


Figure 3. TEM images of the 316L (II) SLM samples structure after heat treatment: bright field and electronic diffraction patterns (a), dark field (b).

Figure 4 shows the diagrams that describe the loading, namely, the ascending curve, and unloading, represented by the distending curve, at the maximum load $F = 0.245 \text{ N}$ as determined by the instrumental microindentation method. It is evident that the heat treatment results in shifting the curves towards higher values of the thrust of the indenter h to the right; consequently the values of the maximal (h_{max}) and residual (h_p) indentation depths rise by 7% and 10% respectively, see table 1. The lower strength properties also prove that the material becomes softer (table 1); namely, the Martens hardness H_M revealing both plastic and elastic deformations decreases by 12%, from $2.72 \pm 0.07 \text{ GPa}$ to $2.39 \pm 0.05 \text{ GPa}$ while the indentation hardness at the maximum load H_{IT} drops by 16% from $3.18 \pm 0.09 \text{ GPa}$ to $2.67 \pm 0.06 \text{ GPa}$. This slight softening of the steel may be attributed to the abovementioned lower density of dislocations following the heat treatment. It is significant to note that the microindentation data shows higher values of the contact elasticity modulus E^* ; it rose by 14% from 171 GPa to 195 GPa (table 1). It reflects a lower porosity (compaction) of the synthesized steel resulting from high temperature heating.

The total mechanical work of indentation W_t determined by the area under the loading curve in figure 4 including the work spent for plastic deformation and elastic recovery, also rises by 8% after heat treatment (table 1), since the less the strength of material, the higher is its deformation under the

indenter and consequently the more work is done on deformation. The work of elastic deformation W_e determined by the area under the unloading curve in figure 4, on the contrary, goes down by 16%. The fraction of the elastic deformation in the total deformation decrease; it is also proved by the lower values of the relation H_{IT}/E^* [8] and the elastic recovery $R = ((h_{max} - h_p)/h_{max}) \times 100\%$ [9] that decrease by 26 and 19%, respectively (table 2). Somehow, the plastic component of the work of indentation calculated using the formula $\delta A = (1 - (W_e/W_t)) \times 100\%$ [10] grows very insignificantly, by 3.5%, and the resistance to deformation after the transition to plastic flow, which is described by the relation $H_{IT} \sqrt{3}/E^* \sqrt{2}$ [11], does not change after heat treatment at all (table 2).

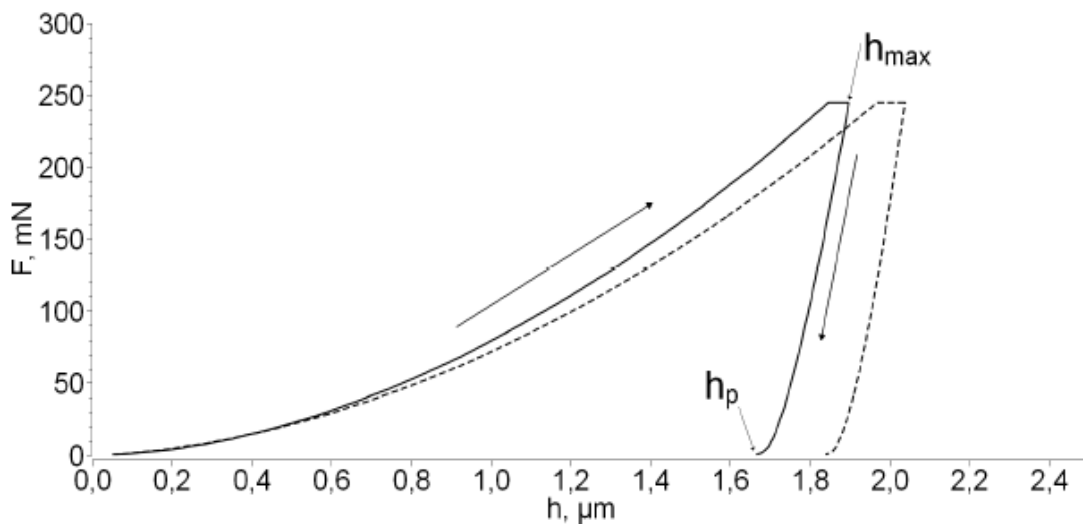


Figure 4. Experimental curves during microindentation of the 316L SLM samples surfaces after (dashline) and without (solid line) heat treatment.

Table 1. The surfaces microindentation results of 316L SLM samples after and without heat treatment.

Treatment	h_{max} (μm)	h_p (μm)	HM (GPa)	H_{IT} (GPa)	E^* (GPa)	W_t (nJ)	W_e (nJ)
Without HT	1.90 ± 0.03	1.67 ± 0.02	2.72 ± 0.07	3.18 ± 0.09	171 ± 4	159.1 ± 2.8	22.0 ± 0.5
After HT	2.04 ± 0.02	1.84 ± 0.02	2.39 ± 0.05	2.67 ± 0.06	195 ± 5	171.8 ± 1.9	18.4 ± 0.4

Table 2. The ability characteristics of 316L SLM samples surface layers to resist mechanical contact action after and without heat treatment.

Treatment	δA (%)	R (%)	H_{IT}/E^*	H_{IT}^3/E^{*2} (GPa)
Without HT	86	12.1	0.019	0.001
After HT	89	9.8	0.014	0.001

The results of the microindentation that have been discussed above support the data on measuring the microhardness applying the recovered indentation technique which shows a slight softening of the SLM steel resulting from the heat treatment. It is shown by lowering the strength characteristics by 5- 16%. In addition, it was found that the fraction of the elastic deformation in the total deformation decreases, indicating a faster transition of the heat-treated steel to plastic deformation under contact loading.

Therefore, the heat treatment that has been applied does not result in strengthening of the steel when the mechanism of aging austenite is employed. Deformation strengthening as well as chemicothermal

treatment leading to chemical modification of the surface layer might prove to be efficient for strengthening austenitic steel synthesized by SLM.

As the authors of the present paper have shown, efficient strengthening and improved tribological properties of metastable and deformation-stable austenitic chrome-nickel steels is achieved by processing with a sliding indenter [12-16] as well as by combining nanostructuring frictional processing with low-temperature plasma nitriding [17-21]. It seems advantageous to use the described modifying processes for making a gradient-strengthened substrate on the surface of the synthesized austenitic steel for further application of nano-compositional thin-film multilayered coatings on the base of amorphous superhard diamond-like carbon and titanium carbides. We will study these directions in our future research, designed to give scientific credence for the new combined method for post-treatment of SLM samples. This method will make it possible to efficiently use thin-film highstrength coatings in additive manufacturing on parts made from structural steels that are significantly inferior in hardness to these coatings.

4. CONCLUSION

The austenitic structure with high densities of dislocations is formed by means of synthesizing a 316L steel by the selective laser melting technique. Heat treatment, quenching from 1050 oC and further 4-hour annealing at 480 oC, performed for degassing, reducing the number of vacancies and relaxing residual stresses do not result in altering the phase composition. However, a lower density of dislocations as well as their configurations in austenitic grains is evident. It causes a slight reduction of micromechanical characteristics to occur: the microhardness goes down by 5%, Martens hardness H_M and indentation hardness at maximum load H_{IT} – by 12 and 16%, respectively. With the help of kinetic microindentation it was determined that the fraction of elastic deformation in the total deformation becomes smaller as caused by heat treatment. A 14% growth of the elasticity modulus E^* was discovered signifying a decrease of the porosity of the steel when heated to a high temperature.

Thus, the studied heat treatment does not provide strengthening through aging austenite in a synthesized steel. To obtain its effective strengthening application of nanostructuring frictional and chemicothermal (plasma nitriding) treatments may turn out to be advantageous as well as additional laying of thin-film coatings on a hardened substrate.

ACKNOWLEDGMENTS

The main results were funded by the RFBR and Sverdlovsk Oblast, project number 20-48-660065. The results of the electron diffraction phase analysis were obtained by the M.N. Mikheev Institute of Metal Physics of the Ural Branch of the Russian Academy of Sciences (IMP UB RAS) within the state assignment of Ministry of Science and Higher Education of the Russian Federation (theme “Structure” No. № AAAA-A18-118020190116-6). The studies were performed at the collaborative access center “Testing center of nanotechnology and advanced materials” of IMP UB RAS.

REFERENCES

- [1] Yap C Y, Chual C K, Dong Z L, Liu Z H, Dong Z L, Zhang D Q, Loh L E and Sing S L 2015 *Appl. Phys. Rev.* 2 041101
- [2] Zhou X, Wang D, Liu X, Zhang D D, Qu S, Ma J, London G, Shen Z and Liu W 2015 *Acta Mater.* 98 1
- [3] Oliver W C and Pharr J M 1992 *J. Mater. Res.* 7 1564
- [4] Amato K N, Gaytan S M, Murr L E, Martienez E, Shindo P V, Hernandez J, Collins S and Medina F 2012 *Acta Mater.* 60 2229
- [5] Pinkerton A J and Li L 2003 *Appl. Surf. Sci.* 208-209 411

-
-
- [6] Bazaleeva K O, Tsvetkova E V and Balakirev E V 2016 *Vestn. Mosk. Gos. Tekh. Univ. im. N.E. Baumana, Mashinostr. (Herald of the Bauman Moscow State Tech. Univ., Mech. Eng.)* 5 117 [in Russian]
- [7] Saeidi K, Gao X, Lofajc F, Kvetkov[†]L and Shen Z J 2015 *J. Alloys Compd.* 633 463
- [8] Cheng Y T and Cheng C M 1998 *Appl. Phys. Lett.* 73 614
- [9] Petrzhik M I and Levashov E A 2007 *Crystallogr. Rep.* 52 966
- [10] ISO 14577-1:2002
- [11] Mayrhofer P H, Mitterer C and Musil J 2003 *Surf. Coat. Technol.* 174-175 725
- [12] Kuznetsov V P, Makarov A V, Osintseva A L, Yurovskikh A S, Savrai R A, Rogovaya S A and Kiryakov A E 2011 *Strengthening Technologies and Coatings* 11 16 [in Russian]
- [13] Makarov A V, Skorynina P A, Osintseva A L, Yurovskikh A S and Savrai R A 2015 *Obrab. Met. (Met. Work. Mat. Sci.)* 4 80 [in Russian]
- [14] Makarov A V, Skorynina P A, Osintseva A L, Yurovskikh A S 2017 *Phys. Metals Metallogr.* 118 1225
- [15] Savrai R A, Makarov A V, Malygina I Yu, Rogovaya S A and Osintseva A L 2017 *Diagnostics, Resource and Mechanics of Materials and Structures* 5 43 [in Russian]
- [16] Makarov A V, Skorynina P A, Volkova E G and Osintseva A L 2020 *Met. Sci. Heat Treat.* 61 764
- [17] Makarov A V, Gavrilov N V, Samoylova G V, Mamaev A S, Osintseva A L and Savrai R A 2017 *Obrab. Met. (Met. Work. Mat. Sci.)* 2 55 [in Russian]
- [18] Makarov A V, Samoylova G V, Gavrilov N V, Mamaev A S, Osintseva A L, Kurennykh T E and Savrai R A 2017 *AIP Conf. Proc.* 1915 030011
- [19] Lezhnin N V, Makarov A V, Gavrilov N V, Osintseva A L and Savrai R A 2018 *AIP Conf. Proc.* 2053 040050
- [20] Makarov A V, Savrai R A, Skorynina P A and Volkova E G 2020 *Met. Sci. Heat Treat.* 62 61
- [21] Zhidkov I S, Kukharensko A I, Makarov A V, Savrai R A, Gavrilov N V, Cholakh S O, and Kurmaev E Z 2020 *Surf. Coat. Technol.* 386 125492

Ultrasonic Welding of Metals: Instruments, Process Parameters, and Prospects of Welding of Ultrafine Grained Materials

**A A Mukhametgalina, M A Murzinova, A A Nazarov, N Yu Parkhimovich,
A A Samigullina, E R Shayakhmetova and A P Zhilyaev**

Institute for Metals Superplasticity Problems, Russian Academy of Sciences, 39 Khalturin st., Ufa
450001, Russia

E-mail: aanazarov@imsp.ru

ABSTRACT

The results of studies on the development of instruments for ultrasonic welding (USW) of metals, which is the basic process for ultrasonic additive manufacturing, are presented. The influence of process parameters (static loading and welding time) on the microstructure and strength of joints produced by USW of commercially pure copper, nickel and titanium is studied. Preliminary results of the first studies on the USW of metals in an ultrafine grained (UFG) state are presented and the prospects of using UFG metals in the ultrasonic additive manufacturing are evaluated.

1. INTRODUCTION

Ultrasonic welding (USW) is a relatively new method of the solid state joining of metals and now is widely used in electrical engineering, electronics, automobile industry etc. for joining foils, plates and wires [1-5]. The interest to USW has increased in the recent years due to an invention of ultrasonic consolidation as one of the methods of additive manufacturing [6-8]. The ultrasonic additive manufacturing is based on successive welding of metallic foils to produce bulk articles. For research needs, this process can also be modeled by means of successive welding of metal sheets using a spot ultrasonic welder. This paper reports the results on the development of instruments for this goal and studies of the structure and properties of joints of three metals, copper, nickel, and titanium, processed by USW with an emphasis on the welding of metals having an ultrafine grained (UFG) microstructure.

Finally, the prospects of using metals with UFG structures in ultrasonic additive manufacturing are outlined.

2. INSTRUMENTS FOR ULTRASONIC WELDING

Ultrasonic horn is a key part of ultrasonic welding equipment, which imparts the ultrasonic energy into the samples of metals under welding. This part must satisfy two main requirements: achieving a sufficient amplitude of vibrations of the welding tip during the welding process, when a significant static load is applied, and the possibility of applying the static load with the least increase of the acoustic resistance. In order to satisfy the former, the horn is made as a kind of ultrasonic concentrator, while the latter condition is satisfied, if the static load is applied at a node. The common way of designing the horns is an analytic calculation (if possible) followed by finite element simulations [9,10].

We have considered three types of horns: 1) a half-wave horn, which has a conical input part and a cylindrical output part which is cut from two sides by vertical surfaces having radial transitions (figure 1 a); 2) a half-wave stepped horn with a radial transition (figure 1 b) and 3) one-wave horn with two radially smoothed steps (figure 1 c). All horns have flattened surfaces for applying a static force and / or

for spanners. As shown by Merkulov [11], a composite horn consisting of a conical input part and cylindrical output part and a stepped horn with an exponential transition section have the highest values of the amplification coefficient. Additional cuts by two vertical surfaces further increases this coefficient for the first type horn. The presence of two stepped transitions provides the third horn also a high amplification coefficient. Khemelev et al. [9] have shown that exponential transition for stepped concentrator can be replaced by a radial one and obtained the correction factors for the lengths of the parts of horns in this case.

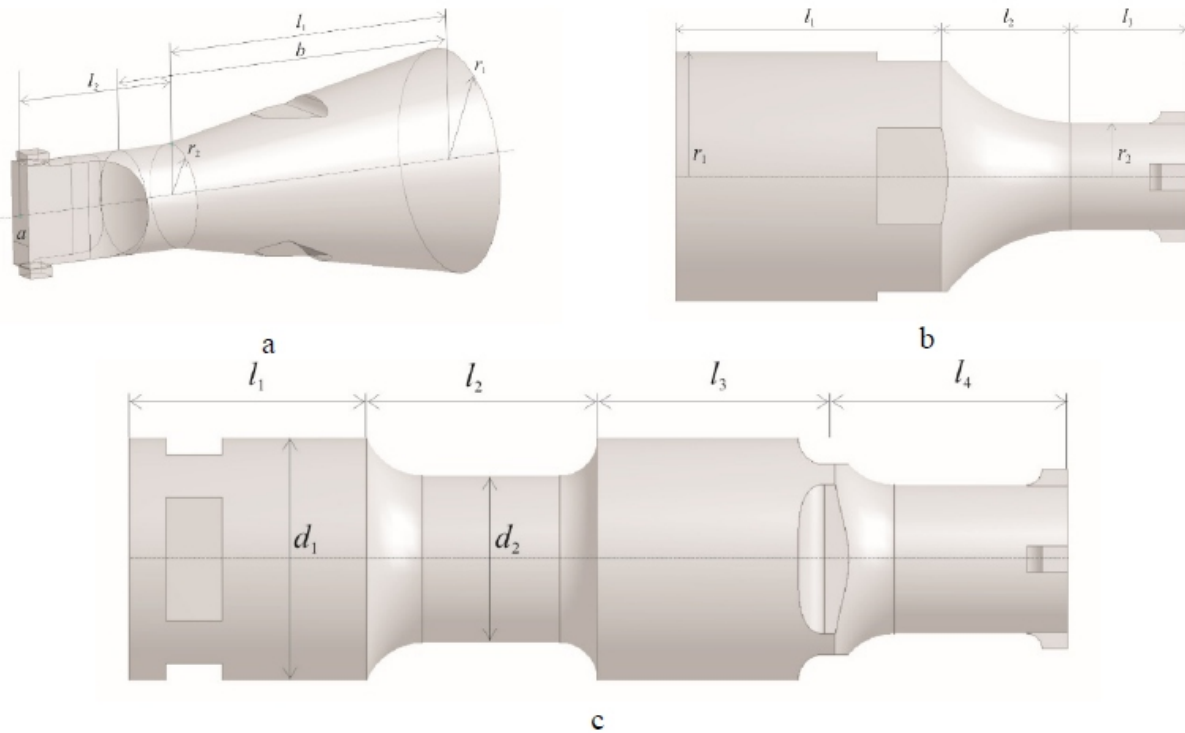


Figure 1. Schemes for design of horns for ultrasonic spot welding: (a) half-wave composite horn consisting of conical input and cylindrical output cut by radial surfaces (type 1); (b) half-wave stepped horn with radial transition (type 2); (c) one-wave stepped with radial transitions (type 3).

The analytic calculations do not allow for a sufficiently accurate prediction of the geometrical parameters of horns, since they are valid for the case of lateral dimensions of horns much less than the longitudinal ones. Also, only numerical calculations of real welding horns having weld tips, flattened surfaces for spanners or static load application, is possible.

Starting from the analytically predicted starting configurations obtained for concentrators without weld tips and flattened surfaces, finite element calculations were done for each type horn. The simulations were carried out for Steel 45, which is widely used for making ultrasonic waveguides. The steel bar to fabricate horns had the following properties: density $\rho = 7826 \text{ kg/m}^3$, Young's modulus $E = 204.25 \text{ GPa}$ and Poisson's ratio $\nu = 0.33$. The calculations were done for the target resonance frequency f in the range of $20.0 - 20.1 \text{ kHz}$. The modal analysis of the horn models was performed using ANSYS Workbench Mechanical 19.1.

For the type 1 horn we have considered a horn with the following geometric parameters: $r_1 = 31.25 \text{ mm}$, $r_2 = 15 \text{ mm}$, $l_1 = 82 \text{ mm}$, $l_2 = 52.5 \text{ mm}$ and different positions of the beginning of radial cuts on the output part of the horn, b . The modal analysis has shown that this type of horn has two neighbor

eigenfrequencies, one of which corresponds to torsional vibrations around the waveguide axis and the other to longitudinal oscillations. Figures 2 a,b present the dependences of these frequencies, f , and the amplification coefficient for longitudinal oscillations, M , of the horns on the values of b . As one can see from the figures, the amplification of the waveguide is very high at small values of b and it decreases with b . However, the use of a horn with an elongated narrow output part would result in a worse transmission of vibrations to the welding tip under static load, and it is better to choose a larger value of b at a reasonable amplification. Also, close frequencies of the two vibration modes should be avoided, otherwise torsional vibrations can be excited along with the longitudinal ones leading to lowering of the resulting amplitude. The choice of $b = 106$ mm can be considered reasonable. Figure 3 represents the displacement map of the horn for this case. One can see that the node of displacements is nicely located on the flattened surface that facilitates applying a static load during USW.

The horn fabricated according to this design, had slightly different sizes (input end diameter 62.5 mm instead of 65 mm, $b = 104$ mm) and the resonance frequency of 20.20 kHz. Recalculation with these parameters yield the frequency 20.22 kHz, i.e. a value very close to the experimental one.

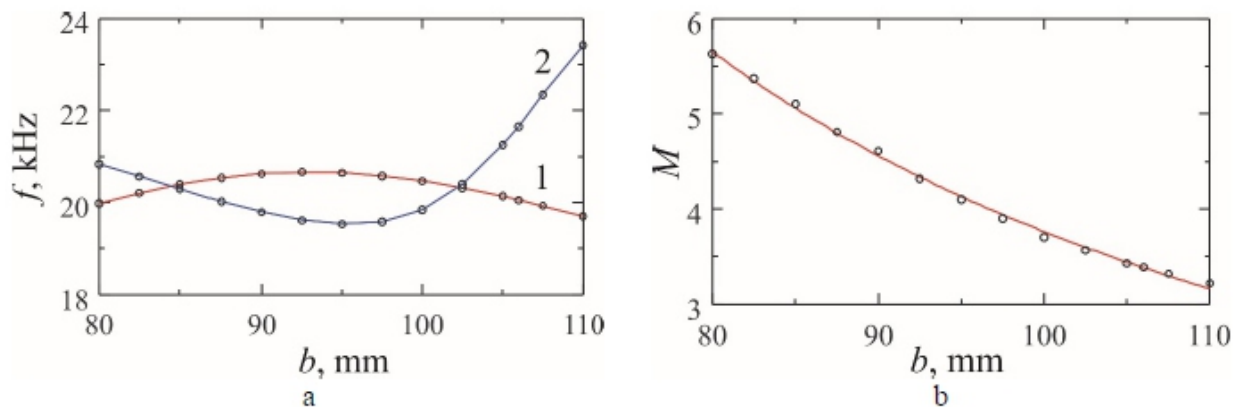


Figure 2. Dependencies of the characteristics of horns of Type 1 on the positions of radial cuts of cylindric parts, b : (a) frequency of longitudinal (1) and neighbor torsional (2) oscillations; (b) amplification ratio for longitudinal vibrations.

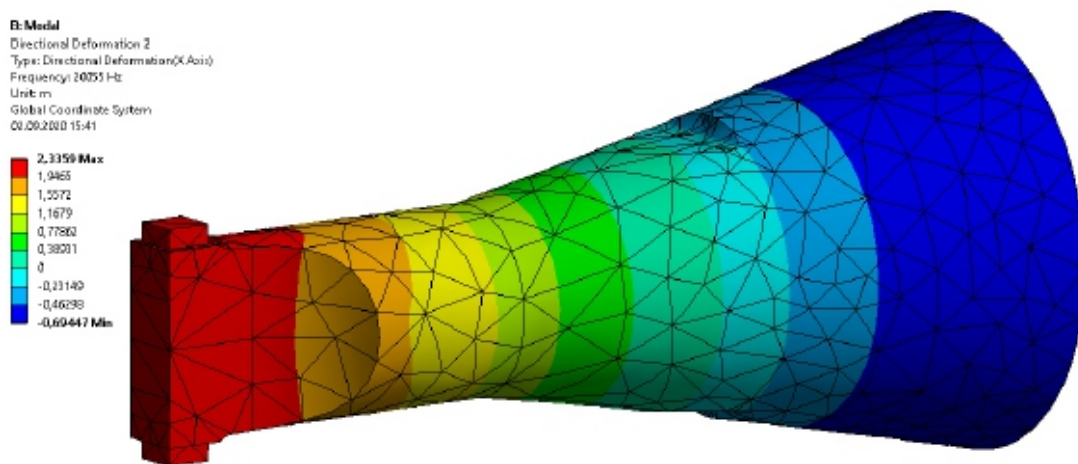


Figure 3. Displacement map of type 1 ultrasonic welding horn with geometrical parameters adjusted for the target frequency.

For the case of type 2 horn, it is important to place the displacement node near the end of the input part, prior to the radial transition. Recently, Khmelev et al. [12] have considered a stepped concentrator with a

mounting flange located at the end of the input part and obtained corrected formulae for the lengths of the parts of the concentrator. In the present case, we looked for a configuration, in which the node is located in the middle of flattened surfaces for spanners and the amplification coefficient is reasonably high. The displacement field for the fitted geometrical parameters, $l_1 = 73.5$ mm, $l_2 = 29$ mm, $l_3 = 37$ mm for $r_1 = 31.25$ mm and $r_2 = 14$ mm is presented in figure 4. One can see that the resonance frequency is in the target interval and the node is located at a place well suited for applying a static load.

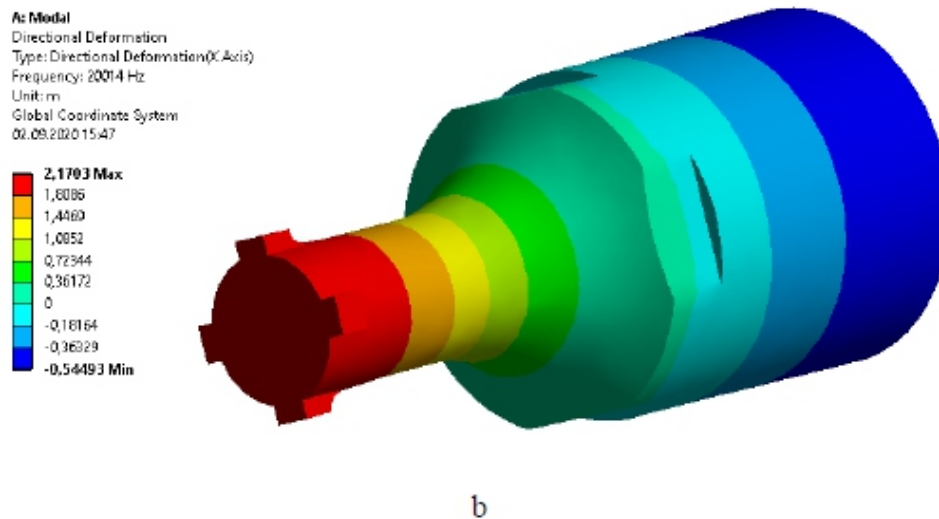


Figure 4. Displacement map of type 2 ultrasonic welding horn with geometrical parameters adjusted for the target frequency.

Figure 5 presents the displacement field map for the type 3 horn designed with the geometric parameters $r_1 = d_1/2 = 31.25$ mm, $r_2 = d_2/2 = 25$ mm, $l_1 = l_3 = 64$ mm, $l_2 = l_4 = 62$ mm. Again, one can see that the displacement node is located at the flattened surfaces near the end of the second large diameter cylinder where the static load can be applied. Despite the smaller ratio between the diameters of the input and output parts, this horn provides the highest amplification coefficient of $M \approx 4.6$.

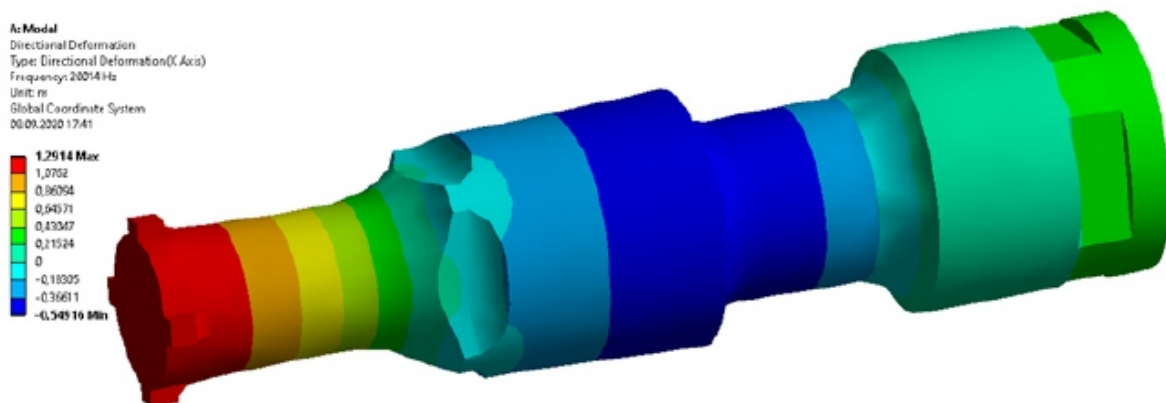


Figure 5. Displacement map of type 3 ultrasonic welding horn with geometrical parameters adjusted for the target frequency.

3. ULTRASONIC WELDING OF COARSE-GRAINED AND ULTRAFINE-GRAINED METALS

Samples of metals (commercially pure copper, nickel, and titanium) with the thickness of 0.5 and 0.7 mm were ultrasonically welded using different regimes of welding given by the values of static load and

welding time at the amplitude of vibrations of the welding tip of about 20 μm . Two types of joint samples were obtained. By welding of two overlapped sheets, samples for lap shear tests were prepared. By successive welding of sheets, which imitated the process of ultrasonic additive manufacturing, consolidated samples were obtained for a structural characterization. Putting thermal couples between the sheets under welding, the temperature rise during welding was evaluated.

As coarse-grained materials, strips cut from as-received commercial sheets of Cu, Ni and Ti with thickness of 0.5 mm were used. To study the role of UFG structure, samples of UFG copper and nickel were processed by high-pressure torsion (HPT). For this, disks of copper and nickel with diameter of 12 mm and thickness of 10 mm were placed between Bridgman anvils with hollows and subjected to torsion straining up to 5 revolutions under the pressure of 6 GPa [13]. As a result of this treatment, disk samples with diameters 12 mm and thickness of 0.7 mm were obtained. This allows one to obtain UFG structures with grain sizes less than 0.5 μm in copper and nickel [14].

Studies have shown that during the USW process a significant increase of the temperature occurs. The maximum temperature increases with static load P and welding time t and can amount from 450°C in copper during welding for 1 s in copper up to more than 700°C during welding for 2 s in titanium.

With an increase of P and t the lap shear strength of USW-processed joints increases. Studies of the microstructure of the joints shows that this is caused by an enhancement of the quality of joints, i.e. the decrease of the density of pores remained in joint interfaces. At the same time, there are optimum values of the static load and above these values the strength of joints decreases due to a significant deformation of the sheets and a change in the failure mode from the interface one to the weld nugget pullout (figure 6).

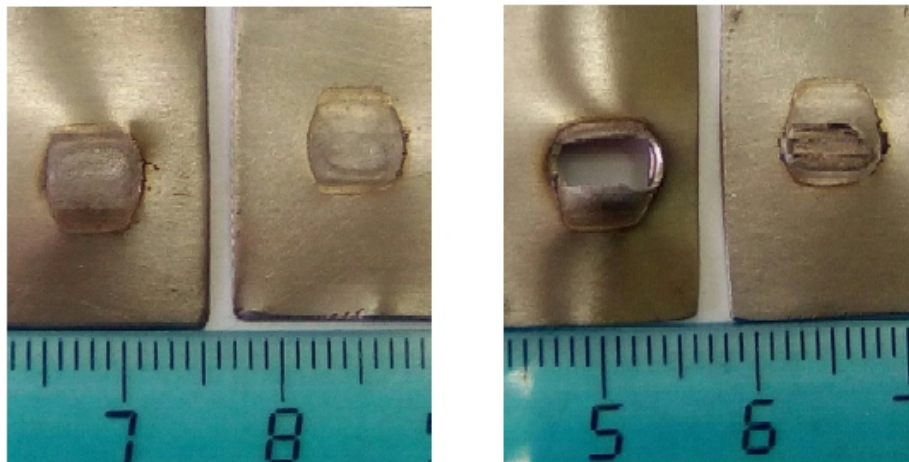


Figure 6. Samples of titanium weld joints processed by USW for 1 s under the static load of 6 (a) and 7 (b) kN after lap shear tests. The left figure indicates the interface failure and the right weld nugget pullout mode of failure.

With an increase of the initial hardness and strength of a material the requirements to the welding parameters providing satisfactory joint quality become more severe: the optimum static load increases and the welding time decreases. This is due to the fact that a higher temperature is required for hard materials to decrease their yield stress and undergo local plastic deformation in the welding zone. For welding of titanium, welding time of 2 s and more was necessary under the load of 5 to 7 kN for the welding tip area of about 30 mm², whereas copper and nickel were well welded at lower loads and in time of 1 s.

The most important preliminary result, which was obtained in the studies is that copper and nickel are ultrasonically welded better in the UFG state than in the coarse-grained one. The joints of UFG copper obtained by USW at static load of 3.5 kN had the same strength of about 33 MPa as the joint obtained by welding of commercial copper sheets under the load of 5 kN. The lap shear strength of the joints processed by USW under the load of 6 kN amounted nearly 100 MPa for UFG nickel versus 70 MPa for commercial nickel.

On the other hand, measurements of the microhardness distribution in the cross section of consolidated samples of nickel show that the minimum microhardness is approximately higher in the material consolidated from UFG samples than in the one processed from commercial sheets. This occurs despite the fact that for the regimes used a significant grain growth occurred in the interface regions during welding of UFG materials (figure 7). Nevertheless, the grain size after consolidation is still in the range of a few micrometers that allows the material to retain its high strength and hardness.

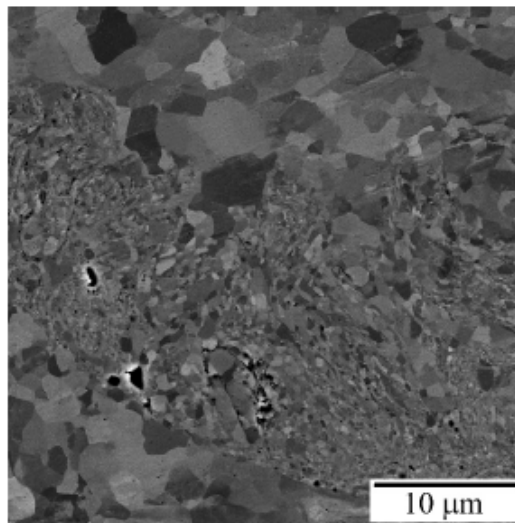


Figure 7. Microstructure of the cross section of a joint of initially ultrafine-grained sheets of copper processed by USW. One can see a significant grain growth near the welding interface.

Thus, the preliminary studies demonstrate that by successive welding, i.e. consolidation of sheets or foils with an UFG structure it is potentially possible to obtain bulk materials, which can have higher strength characteristics than the ones obtained by a consolidation from conventional commercial sheets or foils. In order to make better use of this potential, it is important to look further for regimes of USW, which would provide good joint quality at a less significant grain growth.

A considerable grain growth occurs even in the commercial sheets of titanium, although their initial grain size was out of the ultrafine range. The fact that intensive grain growth occurs in UFG copper and nickel and commercial titanium during the very short time intervals during USW is unusual and calls for more careful studies. Most probably, this is due to an effect of not only the enhanced temperature, but also of an intensive cyclic deformation during the process of ultrasonic welding.

4. CONCLUSIONS

Modal analysis of three types of horns for ultrasonic welding had been performed using finite-element method based ANSYS software. The results show that in some cases (type 1 horn, for example), torsion vibrations modes with very close frequencies can be excited along with the desired longitudinal vibrations and such modes should be avoided in designing the horns.

Experiments have been carried out on USW of the sheets of commercially pure copper, nickel, and titanium. Copper and nickel with an ultrafine grained microstructure were welded ultrasonically for the first time. These preliminary results demonstrate that, despite a significant grain growth in UFG metals due to the effect of high temperature and intensive oscillatory straining, ultrasonically consolidated samples retain a higher microhardness than the samples consolidated from coarse grained metals. This leads to an important conclusion that ultrasonic additive manufacturing based on USW can have a potential in processing bulk articles with higher strength when using materials with an UFG structure..

ACKNOWLEDGMENTS

The present work was supported by the Russian Science Foundation (grant No. 16-19-10126). Electron microscopic studies and mechanical tests were carried out on the facilities of shared services center of IMSPRAS "Structural and Physical-Mechanical Studies of Materials".

REFERENCES

- [1] Silin L L, Balandin G F and Kogan M G 1962 *Ultrasonic Welding* (Moscow: Mashgiz) [in Russian]
- [2] Mitskevich A M 1970 *Ultrasonic metal welding Physical Foundations of Ultrasonic Technology* (Nauka: Moscow) [in Russian]
- [3] Kholopov Yu V *Ultrasonic Welding of Plastics and Metals* (Leningrad: Mashinostroenie) [in Russian]
- [4] Graff K 2005 *Ultrasonic metal welding New Developments in Advanced Welding* ed N Ahmed (Cambridge: Woodhead) p 241-69
- [5] Matheny M P and Graff K F 2015 *Ultrasonic welding of metals Power Ultrasonics-Applications of High-intensity Ultrasound* ed J A Gallego-Juárez and K F Graff (Cambridge: Woodhead Publishing, Elsevier Ltd.) chapter 11 p 259-93
- [6] White D. *Ultrasonic Object Consolidation*. US Patent #6519500, 23 March 2000.
- [7] Graff K E 2011 *Ultrasonic additive manufacturing Welding Fundamentals and Processes* ed. T Lienert, T Siewert, S Babu and V Acoff (Russell Township: ASM Int.) p 731-42
- [8] Herr A and Norfolk M 2019 *Rapid Prototyp. J.* 26/3 445-58
- [9] Khmelev V N, Khmelev S S, Tsyganok S N and Levin S V 2013 *Sources of Ultrasonic Action. Features of Design and Structures* (AltSTU, Biisk) 196 p [in Russian]
- [10] Mukhametgalina A A and Nazarov A A 2019 *Lett. Mater.* 9(4) 414-8 [in Russian]
- [11] Merkulov L G and Kharitonov A V 1959 *Akusticheskii Zhurnal* 5(2) 183-90 [in Russian]
- [12] Khmelev V N, Khmelev S S and Levin S V 2015 *South-Siberian Scientific Bulletin* 2(10) 17-20 [in Russian]
- [13] Khisamov R K, Nazarov K S, Irzhak A V, Shayakhmetov R U, Musabirov I I, Timirayev R R, Yumaguzin Y M and Mulyukov R R *Lett. Mater.* 9(2) 212-7
- [14] Zhilyaev A P and Langdon T G 2008 *Progr. Mater. Sci.* 58 893-979

Nano-Mechanical Testing of Al- Nb Metal Matrix Composites Consolidated by High Pressure Torsion after Annealing

R R Mulyukov^{1,2,3}, K S Nazarov¹, R U Shayakhmetov¹, G F Korznikova¹,
E A Korznikova^{1,4}

¹Institute for Metals Superplasticity Problems RAS, 39 Khalturin St., 450001 Ufa, Russia

²Bashkir State University, 32 Validi st., Ufa, 450076, Russia

³Ufa State Petroleum Technological University, 1 Kosmonavtov st., Ufa, 450064, Russia

⁴Ufa State Aviation Technical University, 12 K. Marx St., 450008, Ufa, Russia

E-mail: elena.a.korznikova@gmail.com

ABSTRACT

Among different approaches for obtaining composite structures, one can distinguish the approach of severe plastic deformation that allows obtaining bulk structures from strongly dissimilar metals. The application of large strains is usually associated with grain refinement and, in some cases, with the formation of intermetallic phases, both factors contributing to the strength characteristics of the material. This work presents an investigation of nanomechanical properties of an Al-Nb composite obtained by high pressure torsion and post deformational annealing. Measurements show that with an increase in the distance from the centre to the edge of the sample, the nanohardness increases from 2.4 to 3 GPa. Young's modulus varies in the range from 182 to 197 GPa, which indicates the non-homogeneity of the composite sample. The Young's modulus of the composite after high pressure torsion was found to be higher than that of pristine Al and Nb, which is probably due to the formation of the intermetallic Al₃Nb phase, having an increased Young's modulus according to ab-initio calculations.

1. INTRODUCTION

Following the general trend of design of new materials with enhanced characteristics, several approaches of obtaining composites have been developed, among them one can recall friction stir welding processing [1], plasma sintering [2], stir casting [3,4], spray deposition [5] and diffusion bonding [6]. However, all mentioned methods are inevitably associated with a local temperature increase which, in turn can lead to inhomogeneity and degradation of the properties of the final product. In this respect, consolidation using severe plastic deformation by high pressure torsion (HPT) has several advantages comparing to other methods, namely, it allows reaching large strains, avoiding the fracture of the sample, the control of the strain rate allows preventing extra heating, and the flexible size of anvils provides an opportunity to vary the shape and size in the moderate range [7–10].

Up to date, the successful rapid diffusion bonding of Al-Mg [11], Al-Cu[12–14] Al-Ni [15] has been reported, where the exceptionally high hardness of the final product is usually associated with the strain induced nucleation of intermetallic phases accompanied by a refinement of the structure refinement.

The loading scheme used in HPT devices allows performing the consolidation of powders of different metals, which also results in the formation of metal matrix composites. This approach enables mechanical alloying of strongly dissimilar materials, such as, Al-Ti [16], Al-W[17] and some others, however the purity of the final product in this case is much lower that for those obtained by consolidation of thin discs. A pioneering attempt to perform bonding of two dissimilar metals - Al and Nb by means of disk consolidation was performed by the authors in [18].

The ability of HPT to the synthesis of bulk composites is primarily associated with a significant inflow of strain energy, which is partially accommodated on the formation of new interfaces, and a high concentration of point defects [19], facilitating diffusion in the lattice. Enhanced diffusion, in turn, provides conditions for the mutual solubility of components and the formation of intermetallic phases at temperatures much lower than those in the corresponding equilibrium phase diagram. The phenomenon of point defect assisted mass transfer in nonequilibrium conditions and related phenomena is addressed in [20-23].

The great number of factors affecting the structure and properties of the composite (the initial structure of the material, HPT processing parameters, number of possible intermetallic phases, exc.) require a great diversity of methods of their characterization. Our previous work reported on the microstructural, X-ray and microhardness investigations of the Al-Nb composite obtained by HPT.

This work is devoted to the analysis of the nano-hardness and the Young's modulus evolution of the studied composite performed on the ultrafine level that allows to uncover new features of the structure evolution upon severe plastic deformation and subsequent annealing, which, in turn, can provide a new insight on the possibilities to create composites with tailorable properties.

2. MATERIALS AND METHODS

Aluminum with a purity of 99.5 wt.% and niobium with a purity of 99 wt.% in the form of disks with a thickness of 0.5 mm and a diameter of 12 mm were used as starting materials for the research. Two disks of aluminum were stacked in the form of a sandwich with one disk of niobium located in the middle. Pressure assisted shear deformation was performed at room temperature on a constrained Bridgeman-type HPT installation with an anvil depth of 0.25 mm at a pressure of 5 GPa with a total number of revolutions $N=30$. Bulk disk-shaped samples of the Al-Nb mixture with a diameter of 12 mm and 0.5 mm thickness were obtained.

Nanomechanical testing has been performed by means of a basic module of the «NanoScan-3D» equipment, which allows performing a comprehensive study of nanomechanical properties in the load range up to 100 mN by indentation and sclerometry methods, and to study surface topography in the semi-contact scanning probe microscopy mode. We have performed the nanoindentation based on the measurement and analysis of the indentation load-displacement data enabling determination of the Young's modulus value and nano hardness of the material by analyzing the load-depth curve (see figure 1) with a load of 30 mN, details of the measurement procedure can be found in [24]. The indentation was performed in three areas ($R=0$, $R=R/2$ and $R=R$, see scheme in table 1) on the cross section of the HPT disc sample. Every value given in table 1 is the result of 5 measurements averaging.

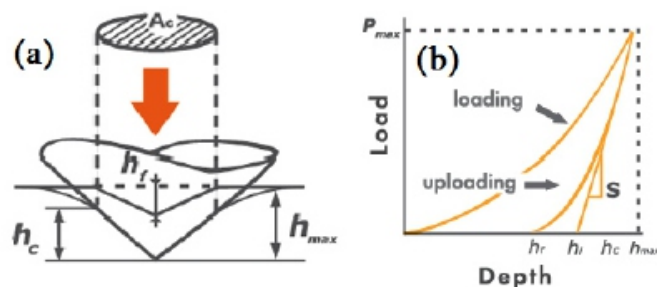


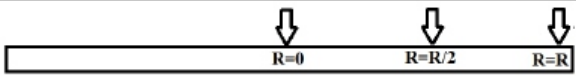
Figure 1. General view of the loading scheme (a), loading curve (b) and contact diagram with the designations of the values used in the method of calculating the modulus of elasticity and hardness. Adopted from [24].

3. RESULTS AND DISCUSSION

Table 1 presents the results of measurements of nanohardness and Young's modulus in the Al-Nb- Al composite after annealing at 400 and 600 °C. The measurements reveal that after annealing at 400 °C the nanohardness grows with the distance from the center to the edge of the sample, while the Young's modulus reveals the opposite dependence - one can see a decrease from 218 to 118 Gpa when moving from the centre to the edge part of the sample. Analysis of nanomechanical characteristics after annealing at 600 °C revealed an overall decrease in all measured characteristics.

Thus, an increase in the annealing temperature resulted in the nanohardness decrease from 3.75 to 3.03 GPa and from 3.26 to 2.44 in the vicinity of the sample edge and the sample center, respectively. From the data presented in table 1, one can also conclude that annealing at 600 °C resulted in the alignment of the Young modulus value along the sample profile, while its overall value was found to be approximately the same as after annealing at 400 °C.

Table 1. The Young's modulus E, and nanohardness H of the composite Al-Nb after annealing

	Al-Nb-Al 400°, 30 min		Al-Nb-Al 600°, 30 min	
	H, GPa	E, GPa	H, GPa	E, GPa
zone				
Sample edge (R=R)	3.75	118.5	3.03	182.45
Middle radius (R=R/2)	2.81	189.75	2.45	196.2
Centre (R=0)	3.26	218.31	2.44	197.74

According to experimental estimations in [25], Young's modulus for Nb in different structural states varies in the range 110-160 GPa, which corresponds to our results. The value of Young's modulus of the composite was higher than that of the original components of the composite. This is probably due to the formation of a large proportion of the dispersed intermetallic phase Al₃Nb, which, according to first-principle calculations has a value of Young's modulus E=260 [25].

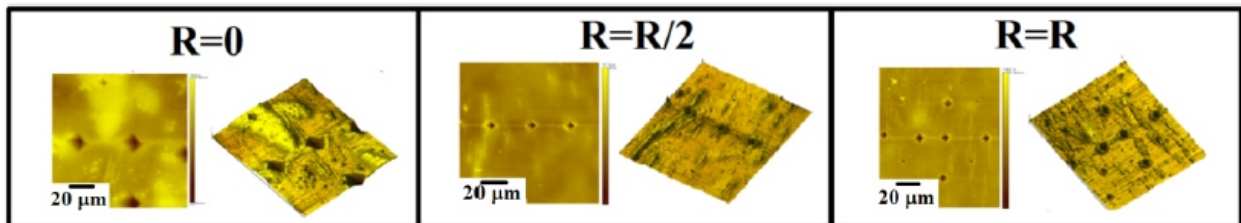


Figure 2. Nanoindentation imprints and corresponding 3D surface profile obtained on the NanoScan- 3D for Al-Nb-Al composite annealed at 400 °C in the center of the sample (R=0) in the middle radius area (R=R/2) and on the edge of the sample (R=R) (see scheme in table 1).

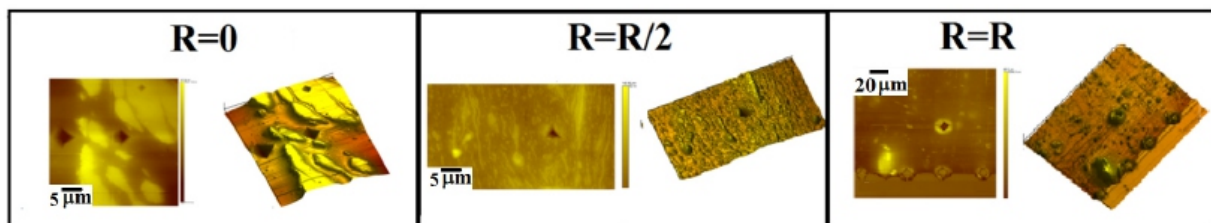


Figure 3. Nanoindentation imprints and corresponding 3D surface profile obtained on the NanoScan- 3D for Al-Nb-Al composite annealed at 600 °C in the center of the sample (R=0) in the middle radius area (R=R/2) and on the edge of the sample (R=R) (see scheme in table 1).

Microstructural investigations of the Al-Nb composite revealed the presence of three main zones along the sample radius, namely a coarse fragment mixture of Al and Nb phases in the center of the sample (at $R=0$), a fine lamellar type structure at the mid radius ($R=R/2$) and a supersaturated solid solution in the vicinity of the disc edge ($R=R$) [18]. Post deformational annealing results in a decrease in the microhardness in $R=0$ and $R=R/2$ areas. Meanwhile the annealing induced precipitation of Al_3Nb phase contributes to the increase of the sample microhardness in the edge region [18].

The analysis of the nanohardness and Young's modulus of the annealed samples is in general in good coincidence with the investigations performed in [18]. Thus, in the center of the disc sample, at $R=0$ for both annealing temperatures 400 and 600 °C (figure 2 a and figure 3 a respectively), one can distinguish separate Al and Nb phases with the size of the imprint in Nb being much smaller than that in Al due to the lower strength of the latter. 2D and 3D images of NanoScan-3D imprints in the cross section of $R/2$ area reveal a laminated structure (figure 2 b and figure 3 b) that correlates well with transmission electron microscopy studies [18]. This structure is stable with respect to annealing at 400 and 600°C, and, as a result one can see that H and E values, as well as the size of the imprint are fairly stable in the studied temperature interval.

The disc edge region ($R=R$) is characterized by a relatively homogeneous microstructure with the highest values of H and E. This can be due to the high fraction of Al_3Nb phase that constitutes ~12% and ~25% after 30 min of annealing at 400 °C and 600 °C, respectively [18]. Since this estimation has been done for the whole sample, the fraction of the intermetallic phase at the periphery of the sample is expected to be even higher, thus considerably contributing to the local mechanical properties of the composite.

4. CONCLUSIONS

The study of the nanomechanical properties of the Al-Nb composite after annealing revealed that an increase in the annealing temperature results in an overall decrease of nanohardness, keeping the gradient of its value along the radius of the sample together with alignment of the Young's modulus value along the radius of the sample. The increased E value of the composite comparing to the pristine Al and Nb components is explained by the enhanced Young's modulus of the Al_3Nb phase formed during HPT and subsequent annealing.

ACKNOWLEDGEMENTS

GFK and RRM gratefully acknowledge the support of the Russian Science Foundation, grant No 18- 12- 00440. The work was partially supported by the State Assignment of Russian Ministry of Science and Higher Education.

REFERENCES

- [1] Mori K, Bay N, Fratini L, Micari F and Tekkaya A E 2013 *CIRP Annals* 62 673–94
- [2] Ujah C O, Popoola A P I, Popoola O M and Aigbodion V S 2019 *Int. J. Adv. Manuf. Technol.* 101 2275–82
- [3] Mistry J M and Gohil P P 2019 *Composites Part B* 161 190–204
- [4] Bihari B and Singh A K 2017 *Int. J. Eng. Res. Appl.* 7 42–8
- [5] Shockley J M, Strauss H W, Chromik R R, Brodusch N, Gauvin R, Irissou E and Legoux J-G 2013 *Surf. Coat. Technol.* 215 350–6
- [6] Kawasaki M, Han J-K, Lee D-H, Jang J and Langdon T G 2018 *J. Mater. Res.* 33 2700–10
- [7] Zhilyaev A and Langdon T 2008 *Progr. Mater. Sci.* 53 893–979
- [8] Kawasaki M, Figueiredo R B and Zhilyaev A P 2020 *Adv. Eng. Mater.* 22 1901386
- [9] Castro M, Pereira P H, Figueiredo R and Langdon T 2019 *Lett. Mater.* 9 541–5

-
-
- [10] Mulyukov Kh Ya, Korznikova G F and Nikitin S A 1996 *J. Appl. Phys.* 79 8584–7
- [11] Kawasaki M, Jung S H, Park J-M, Lee J, Jang J and Han J-K 2020 *Adv. Eng. Mater.* 22 1900483
- [12] Korznikova G, Czeppe T, Khalikova G, Gunderov D, Korznikova E, Litynska-Dobrzynska L and Szlezzynger M 2020 *Mater. Charact.* 161 110122
- [13] Bachmaier A, Rathmayr G B, Bartosik M, Apel D, Zhang Z and Pippan R 2014 *Acta Mater.* 69 301–13
- [14] Korznikova G, Kabirov R, Nazarov K, Khisamov R, Shayakhmetov R, Korznikova E, Khalikova G and Mulyukov R 2020 *JOM* 846 156380
- [15] Edalati K, Toh S, Watanabe M and Horita Z 2012 *Scripta Mater.* 66 386–9
- [16] Sun Y, Aindow M, Hebert R J, Langdon T G and Lavernia E J 2017 *J. Mater. Sci.* 52 12170–84
- [17] Edalati K, Toh S, Iwaoka H and Horita Z 2012 *Acta Mater.* 60 3885–93
- [18] Korznikova G, Korznikova E, Nazarov K, Shayakhmetov R, Khisamov R, Khalikova G and Mulyukov R. 2020 *Advanced Engineering Materials* 2000757
- [19] Korznikova E A, Mironov S Yu, Korznikov A V, Zhilyaev A P and Langdon T G 2012 *Materials Science and Engineering: A* 556 437–45
- [20] Korznikova E, Sunagatova I, Bayazitov A, Semenov A and Dmitriev S 2019 *Letters on Materials* 9 386–90
- [21] Dmitriev S V, Korznikova E A and Chetverikov A P 2018 *Journal of Experimental and Theoretical Physics* 126 347–52
- [22] Zakharov P V, Korznikova E A, Dmitriev S V, Ekomasov E G, Zhou K 2019 *Surface Science* 679 1-5
- [23] Barani E, Korznikova E A, Chetverikov A P, Zhou K, Dmitriev S V 2017 *Physics Letters, Section A: General, Atomic and Solid State Physics*, 381 3553-3557
- [24] Anon <http://nanoscan.info/eng/>, accessed 02.09.2020
- [25] Nong Z, Zhu J, Yang X, Cao Y, Lai Z and Liu Y 2012 *Physica B: Condensed Matter* 407 3555–60

Size- Dependent Phase Stability of Silver Nanoparticles

A M Murzakaev^{1,2}

¹Institute of Electrophysics UB of RAS, 620016, Yekaterinburg, 106 Amundsena St., Russia

²Ural Federal University, 620002, Yekaterinburg, 19 Mira St., Russia

E-mail: Amurzak@mail.ru , Aidar@iep.uran.ru

ABSTRACT

A comparative analysis of the structure of silver nanoparticles obtained by chemical synthesis (citrate method) and electrical explosion of wires is carried out. The structure, phase composition, lattice parameters of silver nanoparticles with sizes from 2 to 50 nm were studied by electron diffraction and high-resolution transmission electron microscopy. All silver nanoparticles obtained by the chemical method have only a cubic structure. Silver nanoparticles obtained by the physical method have cubic and hexagonal structures. The existence of the hexagonal phase under normal conditions is explained by the quenching effect. The lattice parameters of the cubic phase of Ag NPs within the experimental determination error (± 0.01 nm), synthesized by the chemical method and by the method electrical explosion of wires do not differ from each other.

1. INTRODUCTION

Silver (Ag) nanocrystals have been widely used in several areas (catalysis, biological, antimicrobial, information storage, surface-enhanced Raman spectroscopy, interconnects in ultra large-scale integration circuits etc). It is well known that the physical properties of nanoparticles strongly depend on their microstructure. The crystal structure is a critical parameter for the determination of materials properties of the nanocrystals. Silver in its bulk form possesses a cubic crystal structure (Ag-FCC).

The authors of [1] obtained a proof of the presence of a hexagonal phase (Ag-4H) in nuggets of silver. Later it was found that the Ag-4H is a stable phase when the particle size remains smaller than a critical size $d_c < 40$ nm. The stability of the hexagonal polymorph at room temperature and the normal atmospheric pressure has been often discussed in literature as a grain size effect. There are conflicting reports in the literature regarding the phase structure of Ag particles with sizes below 40 nm [2-7]. It is significant that many authors have generally confirmed these results, but the critical size appears to depend strongly on the physical and chemical synthesis techniques.

Changing the size will change the stability range of ordinary bulk materials. This phenomenon has been found in many oxide materials such as ZnO, ZrO₂, Al₂O₃, TiO₂, Fe₂O₃. Various explanations have been proposed for the observed stabilization of the high temperature phase in nanocrystalline oxide particles at room temperature, and controversies still exist in the elucidation of the mechanism of the phase stability. For example, Garvie [8] proposed that the lower surface energy of tetragonal (t) ZrO₂ was the cause for this phase to be present in nanocrystalline form at or below room temperature.

He predicted that particles below about 10 nm in diameter are stabilized in the tetragonal form, and those that are above this critical particle size are subject to the monoclinic (m) transformation. Later, in [9] Murase and Kato suggested that water vapor increased the rate of crystallite growth and decreased surface energy having thus significant effect on the t-m transformation. Domain boundaries were also suggested to inhibit the t-m transformation thus leading to tetragonal phase stability [10]. In [11] Srinivasan et al. argued against the concept proposed by Garvie (stabilization due to lower surface

energy of the t phase) as they found monoclinic particles with much smaller diameters. They suggested that anionic oxygen vacancies present on the surface control the t-m phase transformation on cooling, and that oxygen adsorption triggers this phase transformation. All the articles cited here, except the one by Garvie [8], have in common that the zirconia nanoparticles were produced by various chemical methods (precipitation and calcination). Chemical factors such as adsorbed atoms and purity of raw materials play an important role in the stability of nanocrystalline zirconia and they may completely alter the original surface energy state. Therefore, none of the above explanations have a general validity for pure nanocrystalline zirconia. One of the most recent explanations is based on an increased effective internal pressure due to the surface curvature and the small particle radius (the Gibbs-Thomson effect): $\Delta p = 2\gamma/r$, where Δp is the difference between the external and the internal pressure, γ is the surface energy, and r is the particle radius [12]. This explanation has been since then quite often used for several nanocrystalline ceramic systems as the stabilization of high-temperature or high-pressure polymorph in nanoparticles appeared to be a more general phenomenon. This sizedependent phenomenon is independent of the fabrication method. One of the main quantitative characteristics of nanoparticles is the Gibbs free surface energy. It differs significantly from the energy for macro objects. It has to be mentioned that other mechanisms were also proposed, e.g. a nanothermodynamic model was also established to reveal the origin of the size effect on the polymorphism (face centered cubic and 4H structures) behavior of Ag nanocrystals with the contributions of surface energy and surface stress to the total Gibbs free energy [7]. It shows that the lower surface energy and surface stress coupled with a higher volume of the Gibbs free energy predominates the thermal stability of 4H-structured Ag in a nanometer scale. A thermodynamic explanation has also been developed to calculate the r_c of Ag nanoparticles at different temperatures [7]. The $dc(T)$ function of Ag nanocrystals was also obtained with respect to the thermodynamic consideration of $G_{FCC}(r,T) = G_{4H}(r,T)$. Furthermore, several thermodynamic parameters of the Ag-4H are also determined with the developed model.

In this paper, results of detailed studies on the morphology and crystal structure of Ag nanoparticles produced by chemical method and electrical explosion of wire are presented.

2. EXPERIMENTAL

Silver nanoparticles were synthesized by the physical method using electrical explosion of wire (EEW) as described in detail in [13] and the chemical method using a chemical reduction of $AgNO_3$ with N_2H_5OH in the presence of Na-cit as described in detail in [14]. The minimum size of silver nanoparticles was specially obtained by the chemical method. According to [15], the initial stage of reduction yields clusters Ag^+_2, Ag^+_4, Ag^+_9 , etc. The nascent Ag_x clusters reacted with citrate, which was followed by their aggregation into coarser particles. Upon reaching the critical size (50 - 100 atoms or 1 - 1.5 nm), the clusters virtually cease to grow by the condensation mechanism. Further clusters growth is highly dependent on the citrate concentration. The growth of NPs at intermediate citrate concentrations, namely, $(1-5) \cdot 10^{-4}$ mol litre⁻¹, occurred as a result of reduction of silver ions on the cluster surface. Hence, after the cluster nucleation, its further growth proceeded gradually. Silver NPs formed by this mechanism were unsusceptible to aggregation, spherical and had narrow size distribution. At low citrate concentrations, its stabilizing action was insufficient to prevent the aggregation of clusters, which led to NPs of larger diameters. At higher citrate concentrations, the solution ionic strength reached large magnitudes sufficient for the destabilization of the citrate layer, which also resulted in coagulation. Yellow sol was obtained by boiling solution at $T = 100^\circ C$.

With the use of x-ray phase analysis (D8 DISCOVER diffractometer, Germany), the phase composition, spacing parameters, and the size of the coherent scattering regions (CSR) were determined. The diffractograms were handled with the use of the TOPAS 3 software. The error of determining the content of phases was about 2 wt%. The particle morphology was studied by transmission electron microscopy (TEM) and scanning electron microscopy (SEM) by microscopes JEM-2100 and LEO-982. Selected-area electron diffraction (SAED) and high-resolution transmission electron microscopy HRTEM (JEM 2100) have been used to determine the morphological and phase features of silver nanoparticles. The calibration of the magnification of the HRTEM and the determination of the device constant for the electron diffraction measurements were performed using a gold foil. This choice is due to the fact that the structure of gold is well known, it rarely has defects, and its interlayer distances are 0.23 nm and 0.20 nm (which corresponded to planes (111) and (200) well resolved by the device); in addition, the electron diffraction pattern of gold can easily be interpreted. The processing and analysis of the images were performed using the 3.9.3 version of the Gatan Digital Micrograph program, which allowed us to calibrate images, to apply masks and filters, to perform fast Fourier-transformations (FFT) both of the entire photograph and of the selected regions, to perform measurements, and to save data in various formats. The interplanar distances of the phases of the samples were taken from the Powder Diffraction File.

3. RESULTS AND DISCUSSION

3.1. EEW nanopowders

The electric explosion of a wire represents a rapid change in the physical state of a metal as a result of intense heat generation when a high-density pulse current is transmitted. As a result of the passage of a current pulse, the metal overheats above the melting temperature, and the superheated metal is explosively dispersed. The pressure and temperature at the front of the emerging shock wave reach several hundred megapascals and approximately 10^4 K, respectively. As a result of condensation in a stream of rapidly expanding steam, particles of very small sizes are formed. By adjusting the conditions of the explosion, it is possible to obtain powders with particles of different sizes - from 5 to 300 nm (the weighted average particle radius is 70 nm or more). Results of the XDR analysis of the silver nanoparticles showed that more than 97% mass. had a cubic structure ($a = (0.4082 \pm 0.0007)$ nm) with CSR 21 nm, less than 3 % mass. had a hexagonal structure.

3.2. Chemical nanopowders

The EDX analysis was performed on three sample sites. The analysis showed the absence of possible impurities from elements (N, O) in the samples. From these results, it can be concluded that the silver nanoparticles are pure. The results of the XDR analysis of the silver nanoparticles obtained via the chemical method showed only a cubic structure ($a = (0.4085 \pm 0.0007)$ nm) with a CSR of 10 nm.

Figure 1a shows TEM images of the synthesized silver nanoparticles. It can be observed that the silver nanoparticles have a spherical shape. Both individual nanoparticles and their agglomerates are present in the figure. Figure 1b shows the distribution of nanoparticles by size in yellow sols. The sol contains particles of different sizes - from 2 to 26 nm (the weighted average particle radius is 7 nm). The structure and phase composition of Ag nanoparticles were determined by the SAED method. The inset in figure 1a shows a SAED pattern of the prepared samples. The SAED pattern of the sample has a point-ring shape, which is indicative of the polycrystalline structure of the samples. All nanoparticles are crystalline, no amorphous nanoparticles were detected. The analysis of SAED patterns has confirmed the crystal

structure of particles, which is indexed as a cubic (Fm3m) structure of Ag. An exact determination of the phase composition is possible from the analysis of HRTEM patterns of separate nanoparticles. Figure 1 c, d, e shows three particles of approximately the same size. Figure 1 c shows NPs obtained by the EEW method. The interplanar spacings were obtained from the FFT and they correspond to Ag-4H. In figure 1d,e NPs obtained by the chemical method are shown. The interplanar spacings are obtained from the FFT and correspond to Ag-FCC. After FFT of the whole figure 1e, masking on the FFT, and the reconstructed image by inverting the filtered image is shown in figure 1f. This picture clearly shows Ag clusters ranging in size from 1 to 1.5 nm and NPs up to 5 nm with a cubic structure. The processing of HRTEM images of Ag NPs obtained by the chemical method showed the presence of only the cubic phase. The minimum particle size obtained by the chemical method is an order of magnitude smaller than the particle size obtained by the EEW method.

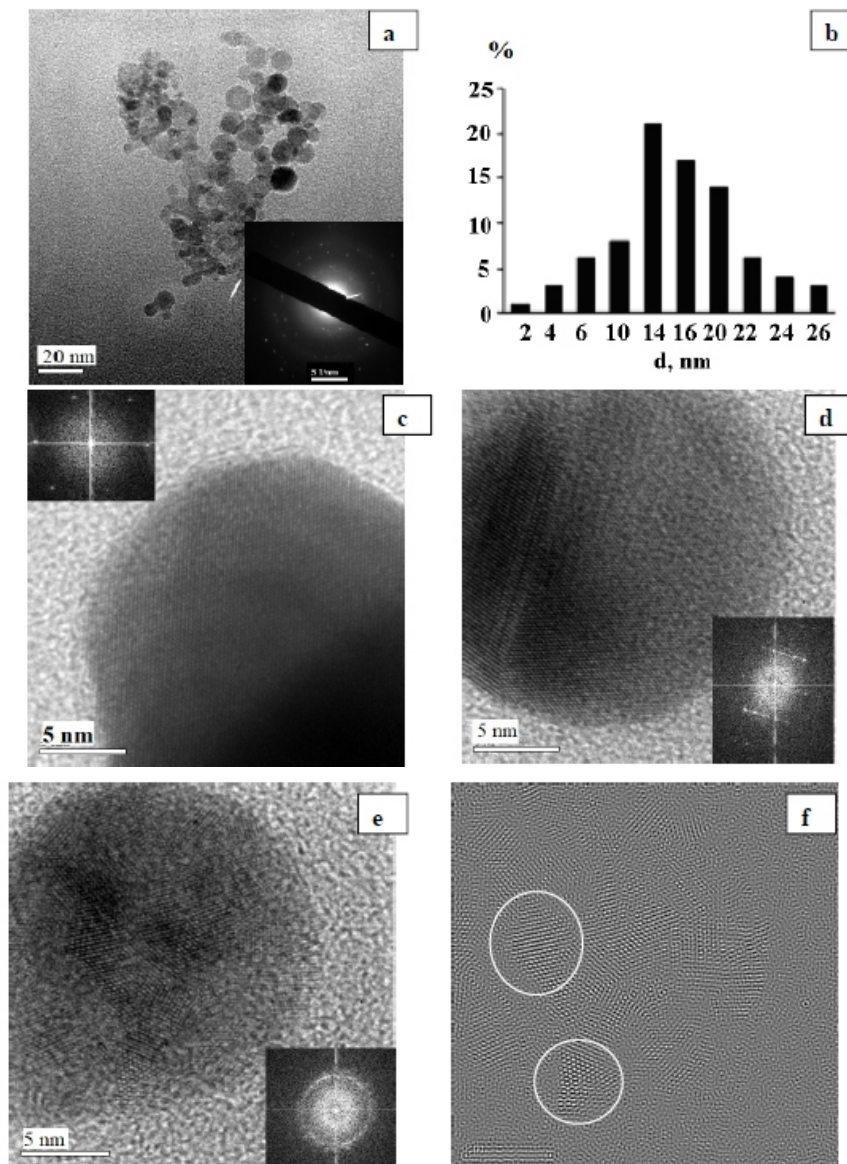


Figure 1.

Despite this, there are no particles with a hexagonal phase among the particles obtained by the chemical method. The presence of Ag-4H in NPs obtained by the EEW method cannot be explained by the Gibbs-Thomson effect. On the other hand, as shown in [7], the $rc(T)$ function decreases with increasing T and leads to a higher thermal stability of Ag-4H than Ag-FCC for small sizes of Ag nanocrystals at lower temperatures and vice versa. Thus, this model does not agree with the obtained experimental data.

Next comes the process of formation of the Ag-4H structure. Solidification of the NPs after EEW comes from undercooling of liquid droplets. The cooling process is extremely short. The crystalline structure firstly formed in the nanoparticle corresponds to the phase diagram of the material and conforms to the temperature at the point in time of nucleus appearance and the increased surface tension of the nanoparticle. The delay in the transformation into a stable lattice take place due to the extremely short cooling process as well as the perfect structure of nanoparticles (Fig. 1c), in which defects, acting as possible nucleation centres, are rare. After cooling at room temperature, lattice transformation is not possible, since the minimum value of energy required for homogeneous nucleation is an insurmountable barrier. As a result, the nanoparticles produced with EEW are “frozen” in the metastable lattice.

Within the experimental determination error (± 0.01 nm), the lattice periods of Ag NPs synthesized by the chemical method and by the method of wire electric explosion do not differ from each other. It has been established that the unit cell parameter of clusters ranging in size from 1 to 1.5 nm and Ag NPs is not a size-dependent quantity and, within the measurement error, takes on a value characteristic of the bulk state. The results obtained contradict the model concepts put forward in [10].

CONCLUSION

Studies using a transmission electron microscope have convincingly shown that Ag NPs obtained by the chemical method have only a cubic structure. Ag NPs obtained by the EEW method contain both hexagonal and cubic phases. Based on the analysis of the conditions for obtaining Ag NPs, the mechanism of stabilization of the hexagonal phase under normal conditions is explained by the quenching effect. The lattice periods of the cubic phase of Ag NPs within the experimental determination error (± 0.01 nm), synthesized by the chemical method and by the electrical explosion of wire do not differ from each other.

REFERENCES

- [1] Novgorodova MI, Gorshkov AI and Mokhov AV 1981 *Int. Geol. Rev.* 23(4) 485
- [2] Bublik AI 1954 *Dokl. Academy of Sciences the USSR* 95 521
- [3] Taneja P, Banerjee R, Ayyub P, Chandra R and Dey GK 2001 *Phys. Rev. B* 64 033405
- [4] Liu XH, Luo J and Zhu J 2006 *Nano Lett.* 6 408
- [5] Liang CH, Terabe K, Hasegawa T and Aono M 2006 *Japan. J. Appl. Phys.* 45(7) 6046-48
- [6] Singh A and Ghosh A 2008 *J. Phys. Chem.* 112(10) 3460
- [7] Yang C C and Li S 2008 *J. Phys. Chem. C* 112(42) 16400
- [8] Garvie RC 1965 *J. Phys. Chem.* 69 1238
- [9] Muraze Y and Kato E 1983 *J. Am. Ceram. Soc.* 66 196
- [10] Mitsuhashi T, Ichihata M and Tatsuke U 1974 *J. Am. Ceram. Soc.* 57 97
- [11] Srinivasan R, Rice L, Davis BH 1990 *J. Am. Ceram. Soc.* 73(11) 3528
- [12] Skandan G, Foster CM, Frase H, Ali MN, Parker JC and Hahn H 1992 *Nanostr. Mater.* 1 313
- [13] Murzakaev A M 2017 *Phys. Met. Metallogr.* 118(5) 459
- [14] Brainina Kh Z, Galperin L G, Kiryuhina T Yu, Galperin A L, Stozhko N Yu, Murzakaev A M and Timoshenkova OR 2012 *J. Sol. St. Electrochem.* 16 2365
- [15] Krutyakov Yu A, Kudrinskiy AA, Olenin A Yu and Lisichkin G V 2008 *Russ. Chem. Rev.* 77(3) 233
- [16] Qi WH and Wang MP 2005 *J. Nanopart. Res.* 7 51

Instructions for Authors

Essentials for Publishing in this Journal

- 1 Submitted articles should not have been previously published or be currently under consideration for publication elsewhere.
- 2 Conference papers may only be submitted if the paper has been completely re-written (taken to mean more than 50%) and the author has cleared any necessary permission with the copyright owner if it has been previously copyrighted.
- 3 All our articles are refereed through a double-blind process.
- 4 All authors must declare they have read and agreed to the content of the submitted article and must sign a declaration correspond to the originality of the article.

Submission Process

All articles for this journal must be submitted using our online submissions system. <http://enrichedpub.com/> . Please use the Submit Your Article link in the Author Service area.

Manuscript Guidelines

The instructions to authors about the article preparation for publication in the Manuscripts are submitted online, through the e-Ur (Electronic editing) system, developed by **Enriched Publications Pvt. Ltd.** The article should contain the abstract with keywords, introduction, body, conclusion, references and the summary in English language (without heading and subheading enumeration). The article length should not exceed 16 pages of A4 paper format.

Title

The title should be informative. It is in both Journal's and author's best interest to use terms suitable. For indexing and word search. If there are no such terms in the title, the author is strongly advised to add a subtitle. The title should be given in English as well. The titles precede the abstract and the summary in an appropriate language.

Letterhead Title

The letterhead title is given at a top of each page for easier identification of article copies in an Electronic form in particular. It contains the author's surname and first name initial .article title, journal title and collation (year, volume, and issue, first and last page). The journal and article titles can be given in a shortened form.

Author's Name

Full name(s) of author(s) should be used. It is advisable to give the middle initial. Names are given in their original form.

Contact Details

The postal address or the e-mail address of the author (usually of the first one if there are more Authors) is given in the footnote at the bottom of the first page.

Type of Articles

Classification of articles is a duty of the editorial staff and is of special importance. Referees and the members of the editorial staff, or section editors, can propose a category, but the editor-in-chief has the sole responsibility for their classification. Journal articles are classified as follows:

Scientific articles:

1. Original scientific paper (giving the previously unpublished results of the author's own research based on management methods).
2. Survey paper (giving an original, detailed and critical view of a research problem or an area to which the author has made a contribution visible through his self-citation);
3. Short or preliminary communication (original management paper of full format but of a smaller extent or of a preliminary character);
4. Scientific critique or forum (discussion on a particular scientific topic, based exclusively on management argumentation) and commentaries. Exceptionally, in particular areas, a scientific paper in the Journal can be in a form of a monograph or a critical edition of scientific data (historical, archival, lexicographic, bibliographic, data survey, etc.) which were unknown or hardly accessible for scientific research.

Professional articles:

1. Professional paper (contribution offering experience useful for improvement of professional practice but not necessarily based on scientific methods);
2. Informative contribution (editorial, commentary, etc.);
3. Review (of a book, software, case study, scientific event, etc.)

Language

The article should be in English. The grammar and style of the article should be of good quality. The systematized text should be without abbreviations (except standard ones). All measurements must be in SI units. The sequence of formulae is denoted in Arabic numerals in parentheses on the right-hand side.

Abstract and Summary

An abstract is a concise informative presentation of the article content for fast and accurate Evaluation of its relevance. It is both in the Editorial Office's and the author's best interest for an abstract to contain terms often used for indexing and article search. The abstract describes the purpose of the study and the methods, outlines the findings and state the conclusions. A 100- to 250-Word abstract should be placed between the title and the keywords with the body text to follow. Besides an abstract are advised to have a summary in English, at the end of the article, after the Reference list. The summary should be structured and long up to 1/10 of the article length (it is more extensive than the abstract).

Keywords

Keywords are terms or phrases showing adequately the article content for indexing and search purposes. They should be allocated heaving in mind widely accepted international sources (index, dictionary or thesaurus), such as the Web of Science keyword list for science in general. The higher their usage frequency is the better. Up to 10 keywords immediately follow the abstract and the summary, in respective languages.

Acknowledgements

The name and the number of the project or programmed within which the article was realized is given in a separate note at the bottom of the first page together with the name of the institution which financially supported the project or programmed.

Tables and Illustrations

All the captions should be in the original language as well as in English, together with the texts in illustrations if possible. Tables are typed in the same style as the text and are denoted by numerals at the top. Photographs and drawings, placed appropriately in the text, should be clear, precise and suitable for reproduction. Drawings should be created in Word or Corel.

Citation in the Text

Citation in the text must be uniform. When citing references in the text, use the reference number set in square brackets from the Reference list at the end of the article.

Footnotes

Footnotes are given at the bottom of the page with the text they refer to. They can contain less relevant details, additional explanations or used sources (e.g. scientific material, manuals). They cannot replace the cited literature.

The article should be accompanied with a cover letter with the information about the author(s): surname, middle initial, first name, and citizen personal number, rank, title, e-mail address, and affiliation address, home address including municipality, phone number in the office and at home (or a mobile phone number). The cover letter should state the type of the article and tell which illustrations are original and which are not.